Analysis and Design Approach for Converters with Large Signal Variations

by

Mohammad Daryaei

A thesis submitted in partial fulfillment for the degree of
Master of Science

in
Energy Systems

Department of Electrical and Computer Engineering
University of Alberta

Abstract

Accurate large signal analysis of Power Electronics converters is essential for achieving high performance and reliable designs. Converter topologies with large signal variations are conventionally analyzed using numerical methods, averaged models, or inaccurate analyses. In this thesis, a Laplace based theorem (LBT) is developed to analyze and derive the steady state response of a class of switching-mode power converters that can be modeled by Ordinary Differential Equation with periodic input. Although LBT is based on Laplace transform which is a linear system analysis tool, it introduces a new tool to analyze a piecewise linear system such as switching power converter. The proposed method is especially useful to analyze resonant converters and has many applications in the design and analysis of such converters and their control systems. The proposed method is applied to a full bridge Series Resonant Converter (SRC) topology with both variable duty cycle and variable frequency control. Using the proposed method continuous/discontinuous conduction modes (CCM/DCM) of SRC are analyzed. Closed form and analytical expressions for converter gain, current phase lag, and ZVS boundary are found and novel optimized converter design approach is proposed without resorting to numerical iterations. The LBT method derivations are compared with existing averaged and inaccurate methods and are also validated by simulations and experimental results.

To the great savior of the world

Acknowledgements

I kindly appreciate my supervisor Dr. Sayed Ali Khajehoddin for his guidance, novel suggestions and feedback to my thesis. I thank him once again for his kind, friendly, and encouraging attitude that makes this collaboration a pleasant and memorable experience.

I would like to thank Mr. Mohammad Ebrahimi for his help and support in my research. Mohammad has helped me a lot in the experimental phase of my thesis and also he had many constructive comments in course of my research development. Also I thank all the UAPEL graduate students for their supports.

I acknowledge the financial support provided by AITF for the whole period of this project.

I express my deepest appreciation to my parents who are the greatest blessings that I have been gifted. Without their encouragement, love and prayers I would never be able to conduct this research and write this thesis.

Contents

List of Tables

List of Figures

Abbreviations

LBT	**L**aplace **B**absed **T**heorem
ODE	**O**rdinary **D**ifferential **E**quation
ZSR	**Z**ero **S**tate **R**esponse
ZIR	**Z**ero **I**nput **R**esponse
USR	**U**nit **S**tep **R**esponse
CCM	**C**ontinuous **C**onduction **M**ode
DCM	**D**iscontinuous **C**onduction **M**ode
SPA	**S**tate **P**lane **A**nalysis
FCA	**F**undamental **C**omponent **A**pproximation
FS	**F**ourier **S**eries
SRC	**S**eries **R**esonant **C**onverter
ZVS	**Z**ero **V**oltage **S**witching
ZCS	**Z**ero **C**urrent **S**witching
EMI	**E**lectro**M**agnetic **I**nterference
PFM	**P**ulse **F**requency **M**odulation
VD	**V**ariable **D**uty cycle

Symbols

ω_s	angular switching frequency	rads^{-1}
f_s	switching frequency	Hz
ω_r	angular resonant frequency	rads^{-1}
f_r	switching frequency	Hz
F	normalized switching frequency	(-)
Q	normalized load quality factor	(-)
n_t	transformer primary to secondary turns ratio	(-)
d	duty cycle	(-)
M	Voltage gain	(-)
θ	current zero crossing angle	(rad)
d_{ZVS}	theoretical ZVS loss duty cycle	(-)
D_{ZVS}	practical ZVS loss duty cycle	(-)
$d_{tripple}$	DCM boundary at ZVS loss duty cycle	(-)
$M_{tripple}$	voltage gain at both DCM and ZVS boundary	(-)
V_{dcm}	capacitor initial voltage at DCM	(V)
ϕ	current interruption angle at DCM	(rad)
φ_d	dead time angle	(rad)

Chapter 1

Introduction

Power converters like any other physiscal system have to be modeled mathematically prior to be anayzed using the mathematical appraoches. Any power converter, consists of switches, sources, and passive elements. In most power converters, the switching actions and sources could be modeled as a periodic and discontinuous input function that is applied to the passive elements network [1–3]. The network's dynamic behavior could be described using an Ordinary Differential Equation (ODE). Thus, the converter is mathematically modeled by an Ordinary Differential Equation (ODE) with periodic and discontinuous input. Figure 1.1 shows a simple converter that is modeled by an Ordinary Differential Equation with periodic and discontinuous input function. Due to the discontinuity of the input function, conventional mathematical approaches of solving ODEs can not be used for exact analysis of the converter. Conventional methods could provide a closed form solution of the ODE if a continuous input function is applied.

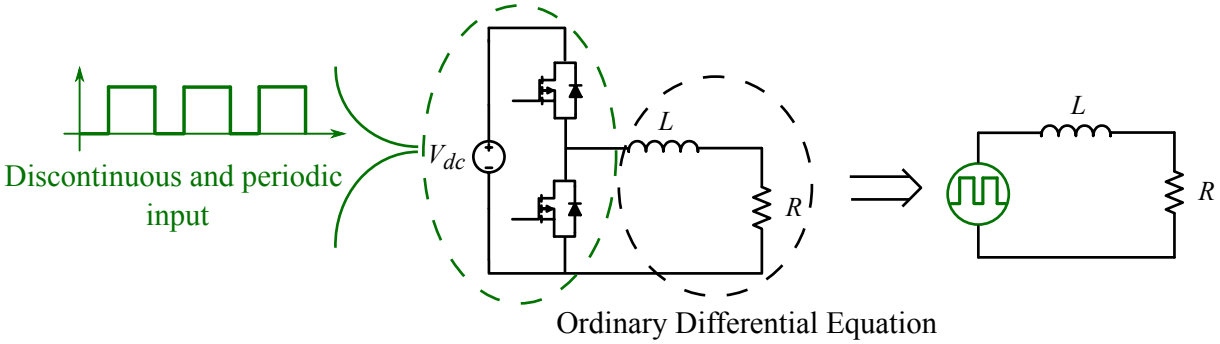

FIGURE 1.1: Simple converter mathematical modeling.

The analysis becomes even more complicated if the converter has two switching stages. DC/DC resonant converters are well-known example that have two switching stages of the inversion and rectification and have a variety of applications. Basically, resonant converters are a suitable candidate for the ever increasing requirements of the emerging applications. To fulfil the requirements of the emerging applications, the switching frequency of power electronics converters is constantly being increased to achieve more compact designs and better performance. The high frequency operation shrinks the size of passive components, and enables compact and high power density power converters. Furthermore, increased switching frequency provides better and fast transient performance that is a crucial feature for the most of emerging applications. However, increasing the switching frequency is limited by the switching frequency loss beyond the tolerable levels. Soft switching converters including resonant converters alleviate the obstacle for high frequency designs such that recent resonant converters can operate in the Very High Frequency (VHF) range [4].

Among all resonant converters, Series Resonant Converter (SRC) is very attractive due to several capabilities: (1) has a simple topology and the parasitics could be integrated in the converter. (2) has flat efficiency against load variations. (3) has fast

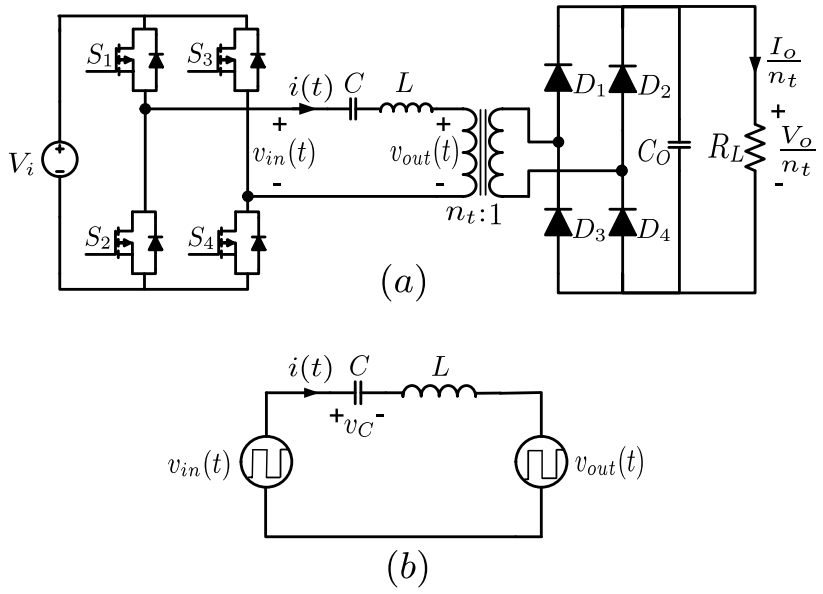

FIGURE 1.2: (a) Topology of the SRC, and (b) SRC equivalent circuit.

transient response because of capacitive output filter. (4) could block the DC component caused by asymmetrical switching or non-idealities [5]. Figure 1.2 shows the topology of the Series Resonant Converter and its equivalent circuit. The converter has two switching stages of the inversion and rectification which are modeled by two switched waveform sources in the equivalent circuit. The output DC voltage and resonant current zero crossing point determine the rectification stage waveform. Since both the output DC voltage and resonant current zero crossing point are functions of input switching waveform, then the source representing the rectification stage is dependent to the input source.

The analysis and design of resonant converters including SRC are among the main challenges which are due to the existence of two dependent switching waveforms [6–10]. Also, because of the poor insight provided by the existing analysis methods, the optimal design of the resonant converters has not been addressed in a clear and efficient manner.

In this chapter different analysis and design methods used for the resonant converters and especially SRC have been reviewed to clearly illustrate the limitations of each method. Ultimately, the proposed method for switched mode power converter analysis (which is also able to analyze the resonant topologies) is introduced and its applications and limitations are discussed.

1.1 Existing Converter Analysis Methods

As the input function of the converter ODE is periodic and discontinuous, conventinal mathematical approaches use infinite series like Bessel functions to analyze the converter. The infinit series and complicated functions are not suitable for the designers and thus other approaches has been used in the literature for converter analysis [11–14]. In the following subsections a brief discussion about each method is presented.

1.1.1 Approximation Methods

As shown in Fig. 1.3, approximation methods, approximate the discontinuous waveform by its fundamental sinusoidal component or a few harmonics of its Fourier series. If the waveform is approximated by its fundmental component (Fundamnetal Component Approximation FCA) then the error would be large and method becomes highly inaccurate. The advantage of the FCA is that it is simple and could provide closed form and parametric equations at the expense of inaccurate results. FCA is a common approach to the analysis of DC/DC resonant converters which approximates all voltage and current waveforms by their fundamental sinusoidal components. Then the rectifier stage is replaced with an equivalent resistance [15]. FCA could be applied

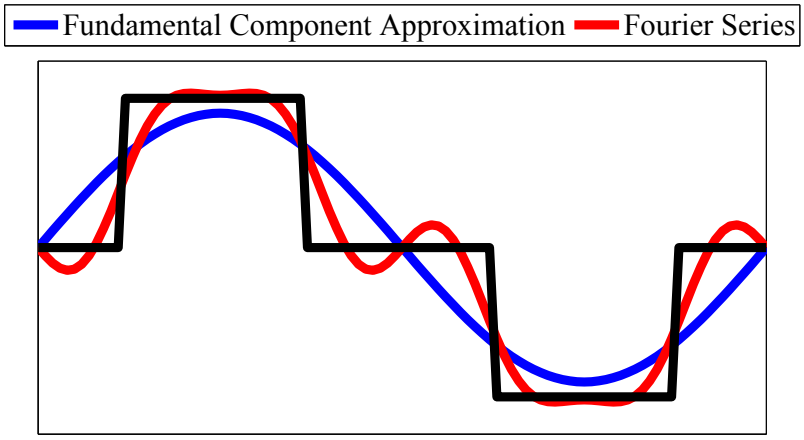

FIGURE 1.3: Approximation methods for converter analysis.

to converters with variable duty ratio and topologies with more than two resonant elements. However, due to sinusoidal approximation, FCA is only applicable to cases operating near resonant frequency with close to unity load quality factors and it is highly inaccurate for other operating conditions. An extended version of FCA is also proposed in the literature and is applied to *LCC* resonant converter [16, 17]. In the extended FCA all waveforms are considered sinusoidal except the parallel capacitor's voltage. This method slightly improves the accuracy for special cases, but it does not provide exact solutions.

A more acccurate analysis approach is Fourier Series that results in infinit series rather than closed form equation [18, 19]. Infinit series are not suitable tool for converter design and its control purposes, thus Fourier Series is a less efficient analysis appraoch. Furthermore, in DC/DC resonant converter analysis if Fourier Series is applied to both rectification and inversion stages, it results in non-linear equations [20]. Thus, Fourier Series could only be applied to the inversion stage and the rectifier stage is replaced by its equivalent resistance obtained from FCA method.

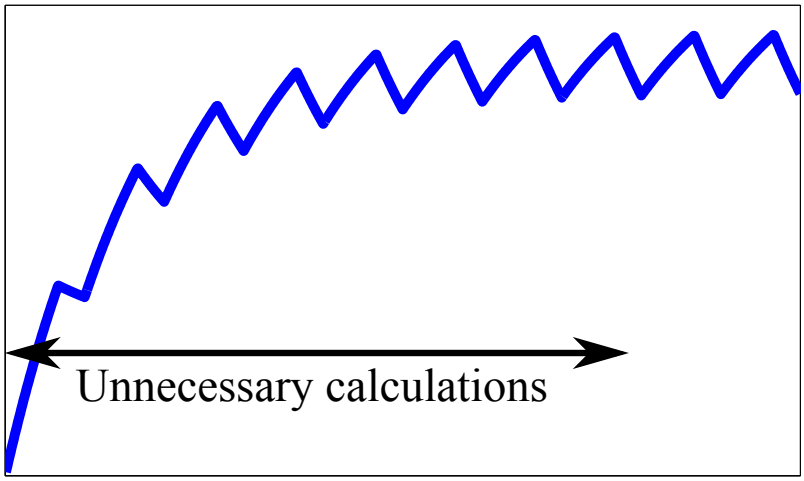

FIGURE 1.4: Numerical period to period analysis of the converter.

1.1.2 Numerical Methods

The numerical methods that are commonly used in simulation softwares could not provide the parametric or even closed form solutions, however, they are very accurate. Basically, these methods numerically solve the ODE with a given initial condition from period to period and update the initial condition at the beginning of each period until they reach the steady state conditions. Therefore, numerical methods are cumbersome but accurate analysis tool that do not provide any parametric or closed form equation needed for design [13, 14]. Figure 1.4 shows the period to period analysis of the numerical methods that has a lot of unnecessary calculations to reach the steady state response.

1.1.3 Time domain methods

For the time domain analysis, first initial conditions of the converter are assumed to be unknown parameters, then ODE of the converter is solved for one switching cycle.

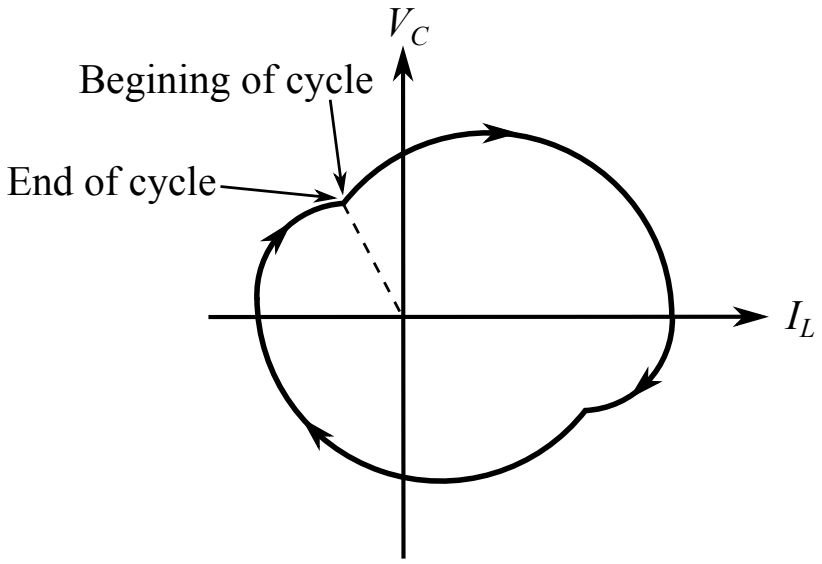

FIGURE 1.5: State Plane Analysis approach for the resonant converters.

By equating the states of the converter at the beginning and end of the switching cycle the steady state response of the converter is obtained. As the time domain response of the high order or variable duty cycle converters is complex, the time domain method for these converters normally leads to non-linear equations. Therefore, no closed form equation for the converter waveform is obtained [21–24].

State Plane Analysis (SPA) is a time domain method that is used for DC/DC resonant converter analysis [25, 26]. SPA has been used for analysis and design of simple resonant converters [27]. SPA is used to analyze the square wave operation of series resonant converter (SRC) as well as parallel resonant topologies[28]. Figure 1.5 shows the SPA approach used for square wave operation analysis of second order resonant converters. In this approach the state trajectories of the converter states are sketched for a single cycle and by equating the states at the beginning and the end of cycle, closed form equations for converter operation is obtained. SPA method provides accurate results, however, its application is limited due to following reasons. Firstly, it

is only applicable to converters with symmetrical square wave inputs. If other modulating schemes like phase shifted PWM (variable duty ratio) are used SPA cannot be applied. Secondly, the method is based on the graphical analysis and can not be used for resonant topologies with more than two passive components or if the Equivalent Series Resistance (ESR) of resonant components is included in the model.

In summary, to the best of our knowledge, there is no analysis for power converters with variable duty ratio that could provide parametric and accurate equations suitable for optimal design and control.

1.2 Series Resonant Converter (SRC) Design

Due to the poor insight provided by conventional methods applied to the SRC, the trade-offs in the design either have not been observed or have not been addressed in a clear way. Among the conventional analysis the methods that result in more accurate results or closed form equations (however non-linear and implicit), could be used to achieve better designs.[29–31]. Authors in [29] have used a tedious time domain analysis approach for *LCC* resonant converter and have improved the accuracy by considering the charge and discharge time for the parallel capacitor. The improved accuracy along with suitable normalization have facilitated the reduction of component stress for the proposed design procedure. In [30, 31] time domain analysis of the *LLC* resonant converter has led to closed form but nonlinear sets of equations. Then, derived equations are proposed to reduce the number of iterations in the optimum design loop.

1.3 Thesis Motivations

The main objective of this thesis is to obtain a parametric and accurate analysis tool for power converters in general and then apply the method to Series Resonant Converter to achieve an effective analysis tool and optimum design. Motivations of this thesis are briefly presented as below.

1.3.1 Accurate and Parametric Analysis Tool

The first motivation of this study is to propose a new analysis tool that provides:

1) Steady state solutions for the converter ODE with discontinuous and periodic input.

2) parametric and closed form solutions.

A mathematical theorem based on Laplace transform is presented to propose the new analysis methodology. The proposed method, firstly finds the steady state initial conditions with the proposed Laplace Based Theorem (LBT) and then solves the converter ODE with the steady state conditions for only one period. Zero Input Response of the ODE could be easily derived using the obtained steady state conditions. However, due to the discontinuity of the input function, Zero State Response of the system will be changed at each discontinuity point. The input function behavior at discontinuity points is described as a step function. Therefore, the unit step response addition is used to reflect the discontinuity effects on Zero State Response.

1.3.2 Variable Duty Cycle SRC Analysis

As discussed earlier, parametric and accurate analysis of the variable duty cycle SRC has never been addressed in the literature due to the presence of two dependent discontinuous sources that makes the converter ODE non-linear. Therefore, second motivation of this study is the accurate and parametric analysis of variable duty ratio Series Resonant Converter. For the analysis of the variable duty ratio SRC, first two intermediate variables of voltage gain and current zero crossing angle are defined to make the two discontinuous sources independent and remove the non-linearity problem. Then, using the proposed method SRC is analyzed and intermediate variables that were defined to remove the non-linearity problem are obtained in terms of main variables of the converter.

1.3.3 SRC Design

The third motivation of this study is to present a novel design for the SRC that is based on accurate and closed form equations rather than iterative loops or approximations. Since there is no closed form equation provided by conventional methods, the existing design procedures use iterations to find optimum design. Also conventional design procedures ignore the dead-time effect on switching losses and effect of current waveform distortions caused by discontinuous input function. In this thesis, the accurate current waveform is used to propose the new design procedure and the dead-time effects on the switching loss and Zero Voltage Switching operation are discussed. Also as the proposed method has provided closed form equations for the SRC characteristics, the closed form selection criteria is obtained for each parameter.

There are three methods for SRC control as below: 1) frequency control. 2) duty cycle control. 3) both duty cycle and frequency control. The control method affects the design procedure and thus, systematic design procedure is proposed for each control technique.

1.4 Thesis Outline

Chapter 2 of the thesis the presents the proposed Laplace Based Theorem (LBT) along with mathematical proof of the theorem. Then a procedure is presented to apply the LBT to power converters. The procedure is illustrated using a simple RL circuit. The proposed method is then applied to a buck converter and different forms of the response are analyzed to obtain exact waveforms with ripple content. The obtained waveforms could be used to obtain boundary condition for DCM and also to investigate the ripple cancellation methodologies.

In chapter 3 a brief description of the SRCs and their operating principal is presented. The inherently nonlinear differential equation of the SRC is obtained for steady state equivalent circuit. Intermediate variables are defined to decompose the nonlinear differential equation into two ODEs. ODEs are solved using the proposed method and the intermediate variables are found in terms of main variables. Both CCM and DCM operation of the SRCs are analyzed and closed form equations are derived for ZVS and DCM boundaries. The results of the proposed method is compared to the existing methods and it is shown that in addition to parametric analysis the proposed method provides more accurate results. Ultimately the derivations of the proposed method are validated by means of both simulation and experimental results.

In chapter 4 two different approaches for SRC control are discussed (Pulse Frequency Modulation and Variable Duty Ratio control). Using the insight provided by the proposed method, the design trade-offs for each case are presented. A clear and parametric equation is proposed for selection of each parameter. Then, a systematic design flowchart is presented for each case that is based on definite equations rather than cumbersome iterative solutions. Finally the improvements that could be obtained by combining both of the methods are discussed.

Chapter 2

The Proposed Theorem and Analysis Method

Most of the switched mode power converters, can be modeled by an ODE with discontinuous and periodic input. Classical methods either average the input function to solve the discontinuity issue or they use infinite number of continuous functions to estimate the discontinuous signal. In this thesis the discontinuities caused by switching actions are handled by a theorem proposed based on the Laplace transformation. The new theorem is based on a linear system analysis theory (Laplace transform) and introduces a new tool to analyze a piecewise linear system such as that of a power converter. The Laplace Based Theorem (LBT) is firstly introduced and proved in section 2.1, then the procedure of converter analysis with LBT is described using simple RL circuit and buck converter in section 2.2.

2.1 The Laplace Based Theorem (LBT)

Laplace Based Theorem (LBT) is proposed to predict an accurate periodic solution of the ODE, where the changes caused by the discontinuous switching input function are accurately predicted at steady state condition. The solution of every ODE consists of zero state response and zero input response that are respectively caused by input function and initial conditions. Both, zero state response and zero input response may have the transient part and steady state part. In the newly proposed method the initial conditions at the start of every cycle are determined such that the transient response caused by the input function is compensated and system response becomes purely periodic. Therefore, using LBT, an accurate steady state response is achieved by finding such initial conditions.

Laplace Based Theorem. *Assume $P(D)x(t) = f(t)$ is an n-th order ODE where, $D = \frac{d}{dt}$ is the differentiation operator, and $P(.)$ is the characteristic polynomial:*

$$P(D) = \sum_{k=0}^{n} a_k D^k$$

The characteristic polynomial has n roots which are denoted by s_j. Also, $f(t)$ is a periodic input with period T that can have any finite number of discontinuities and $x(t)$ is the ODE response.

(i) Laplace transform of the ODE results in $P(s)X(s) - G(s) = F(s)$, where $P(s)$ is the characteristic polynomial in Laplace domain for which differentiation operator has been changed to Laplace variable s, and $F(s)$ is the Laplace transform of the input function:

$$F(s) = \frac{\int_0^T f(t)e^{-st}dt}{1 - e^{-sT}}$$

And $G(s)$ is a function of initial conditions of $x(t)$:

$$G(s) = x_0 a_n s^{n-1} + (x_0 a_{n-1} + x_1 a_n) s^{n-2} + ... = \sum_{k=0}^{n-1} b_k s^k \tag{2.1}$$

$$x(0) = x_0,\ x^{(1)}(0) = x_1,\ ..., x^{(n-1)}(0) = x_{n-1}$$

.

(ii) By solving n equations of $G(s_j) = -F(s_j)$ $j = 1, \ldots, n$, the n unknown initial conditions $x_0,\ x_1,\ ..., x_{n-1}$ can be calculated so that $x(t)$ becomes purely periodic in steady state without any transient response. In case of identical roots, the distinct equations are obtained by equating the derivatives of $F(s)$ and $G(s)$ at the multiple root. Consider $s = a$ is the root of $P(s)$ with multiplicity of m. In order for $x(t)$ to become purely periodic, followings are necessary.

$G^{(m-1)}(a) = -F^{(m-1)}(a)$, $G^{(m-2)}(a) = -F^{(m-2)}(a)$, ..., $G'(a) = -F'(a)$, $G(a) = -F(a)$.

Proof. In order to prove the theorem it is assumed that $x(t)$ is the steady state periodic solution, then the necessary condition for this to actually happen, is obtained. $x_{1p}(t)$ is defined to be the truncated version of $x(t)$ which is equal to $x(t)$ for $0 \leq t < T$ and zero anywhere else. Since $x(t)$ is the steady state periodic solution its Laplace transform is:

$$X(s) = \frac{X_{1p}(s)}{1 - e^{-sT}} \tag{2.2}$$

Therefore, following equation happens for a periodic $x(t)$.

$$X_{1p}(s) = X(s).\left(1 - e^{-sT}\right) \tag{2.3}$$

The necessary condition for this to happen is obtained by plugging the $X(s)$ obtained from ODE Laplace transform into (2.3) and then finding the expression for $x_{1p}(t)$. The $X(s)$ obtained from ODE Laplace transform is:

$$X(s) = \frac{G(s)}{P(s)} + \frac{F(s)}{P(s)} \tag{2.4}$$

If (2.4) is substituted in (2.3):

$$X_{1p}(s) = \frac{G(s)}{P(s)}\left(1 - e^{-sT}\right) + \left[\frac{1}{P(s)}\right].\left[F(s)\left(1 - e^{-sT}\right)\right] \tag{2.5}$$

Since $F(s)\left(1 - e^{-sT}\right) = F_{1p}(s)$:

$$X_{1p}(s) = \frac{G(s)}{P(s)}\left(1 - e^{-sT}\right) + \left[\frac{1}{P(s)}\right].\left[F_{1p}(s)\right] \tag{2.6}$$

$$X_{1p}(s) = \frac{G(s)}{P(s)} - \frac{G(s)}{P(s)}e^{-sT} + \left[\frac{1}{P(s)}\right].\left[F_{1p}(s)\right] \tag{2.7}$$

Taking inverse Laplace from both sides results in:

$$x_{1p}(t) = L^{-1}\left\{\frac{G(s)}{P(s)}\right\} - L^{-1}\left\{\frac{G(s)}{P(s)}e^{-sT}\right\} + L^{-1}\left\{\left[\frac{1}{P(s)}\right].\left[F_{1p}(s)\right]\right\} \tag{2.8}$$

Consider s_j are roots of the characteristic equation $P(s) = 0$, using the Heaviside expansion theorem followings are obtained.

$$L^{-1}\left\{\frac{G(s)}{P(s)}\right\} = \sum_{j=1}^{n} \frac{G(s_j)}{P'(s_j)} e^{s_j t} u(t) \tag{2.9}$$

$$L^{-1}\left\{\frac{1}{P(s)}\right\} = \sum_{j=1}^{n} \frac{1}{P'(s_j)} e^{s_j t} = h(t) \tag{2.10}$$

$$L^{-1}\left\{\frac{1}{P(s)} F_{1p}(s)\right\} = h(t) * f_{1p}(t) = \int_0^t f_{1p}(\tau) h(t-\tau) d\tau = \int_0^t f_{1p}(\tau) \sum_{j=1}^{n} \frac{e^{s_j(t-\tau)}}{P'(s_j)} d\tau \tag{2.11}$$

If (2.9) and (2.11) are substituted in (2.8):

$$x_{1p}(t) = \sum_{j=1}^{n} \frac{G(s_j)}{P'(s_j)} e^{s_j t} u(t) - \sum_{j=1}^{n} \frac{G(s_j)}{P'(s_j)} e^{s_j(t-T)} u(t-T) + \int_0^t f_{1p}(\tau) \sum_{j=1}^{n} \frac{e^{s_j(t-\tau)}}{P'(s_j)} d\tau \tag{2.12}$$

For $t > T$, $f_{1p}(t) = 0$ and:

$$\int_0^t f_{1p}(\tau) \sum_{j=1}^{n} \frac{e^{s_j(t-\tau)}}{P'(s_j)} d\tau = \int_0^T f_{1p}(\tau) \sum_{j=1}^{n} \frac{e^{s_j(t-\tau)}}{P'(s_j)} d\tau = \sum_{j=1}^{n} \frac{e^{s_j t}}{P'(s_j)} \int_0^T f_{1p}(\tau) e^{(-s_j \tau)} d\tau \tag{2.13}$$

Therefore $x_{1p}(t)$ for $t > T$ is:

$$x_{1p}(t) = \sum_{j=1}^{n} \frac{G(s_j)}{P\acute{(}s_j)} e^{s_j t} - \sum_{j=1}^{n} \frac{G(s_j)}{P\acute{(}s_j)} e^{s_j(t-T)} + \sum_{j=1}^{n} \frac{e^{s_j t}}{P\acute{(}s_j)} \int_0^T f_{1p}(\tau) e^{(-s_j \tau)} d\tau \quad (2.14)$$

$$x_{1p}(t) = \sum_{j=1}^{n} \frac{e^{s_j t}}{P\acute{(}s_j)} \left[G(s_j) \left(1 - e^{-s_j T}\right) + \int_0^T f_{1p}(\tau) e^{(-s_j \tau)} d\tau \right] \quad (2.15)$$

As it can be seen for $t > T$, $x_{1p}(t)$ is the summation of some exponential terms. Since $e^{s_j t}$ are linearly independent functions then $x_{1p}(t)$ is zero for $t > T$ if and only if all the coefficients of the exponential terms are equal to zero:

$$\left[G(s_j) \left(1 - e^{-s_j T}\right) + \int_0^T f_{1p}(\tau) e^{(-s_j \tau)} d\tau \right] = 0 \quad (2.16)$$

$$G(s_j) = -\frac{\int_0^T f_{1p}(\tau) e^{(-s_j \tau)} d\tau}{(1 - e^{-s_j T})} \quad (2.17)$$

$$G(s_j) = -F(s_j) \quad (2.18)$$

Therefore, $x(t)$ is the periodic solution of the ODE if and only if $G(s_j) = -F(s_j)$ for $j = 1, \ldots, n$.

□

2.2 The Proposed Procedure for Converter Analysis

It is important to note that LBT is applicable to the converters that could be modeled by an ODE with periodic input. There may be some converters that cannot be modeled by ODE and in fact, the coefficients of their differential equation are time variant. However, a large class of the power converters are modeled by an ODE with periodic and discontinuous input. In this case, system is linear and thus the Laplace Based Theorem could be used to analyze them and solve the discontinuity problem caused by switching actions. In order to apply the LBT to these converters, the following steps must be taken.

1. Obtain the ODE of the converter passive components.
2. Find $F(s)$, the Laplace transform of the input switching waveform $f(t)$.
3. Find $G(s)$ function using (2.1), assuming $x_0, \ldots, x_{n-1}$ are the n unknown initial conditions.
4. Form the following n set of equations $G(s_j) = -F(s_j)$ for all roots of $P(s)$, and then solve them to find $x_0, \ldots, x_{n-1}$.
5. Now that the initial conditions at the start of each period at steady state are known, solve a new ODE $P(D)x_{1p}(t) = f_{1p}(t)$ using the calculated initial conditions to find $x_{1p}(t)$. Note that $x_{1p}(t)$ is one period of the solution and similarly $f_{1p}(t)$ is one period of the input and as such the new ODE can be easily solved.

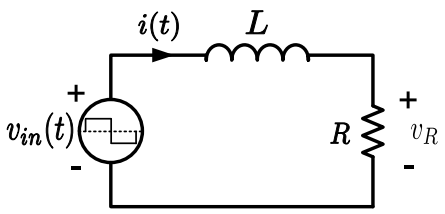

FIGURE 2.1: Simple RL circuit with square wave input.

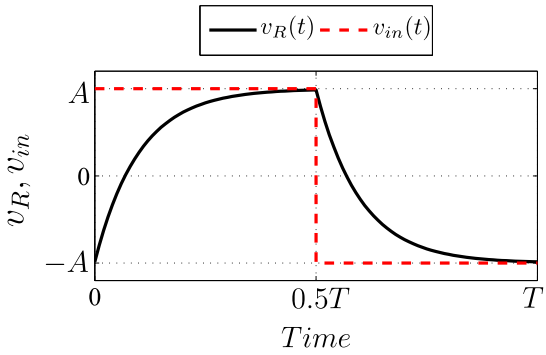

FIGURE 2.2: Obtained $v_R(t)$ using the proposed method.

Solution of the new ODE, $x_{1p}(t)$, is equal to the desired signal $x(t)$ for $0 \leq t < T$ and equal to zero anywhere else. Similarly $f_{1p}(t)$ is equal to $f(t)$ for $0 \leq t < T$ and zero anywhere else. As it has been proved, $x_{1p}(t)$ will be equal to zero for $t > T$ because all n equations of $G(s_j) = -F(s_j)$ hold.

In $P(D)x_{1p}(t) = f_{1p}(t)$, the input function is discontinuous and the response is separated into zero state response and zero input response. The zero input response is simply obtained by solving the homogeneous ODE with the obtained steady state initial conditions. For zero state response it is important to note that from mathematical point of view the discontinuous input function is the summation of some unit step functions that start at discontinuity points. Therefore, the unit step response of the system first has to be obtained. Then, according to the discontinuity points the unit step responses with appropriate amplitude are shifted and summed up to achieve the zero state response. Now, the zero state response and zero input response can be added to obtain the complete steady state response.

2.3 Simple RL Circuit Example

In order to illustrate the procedure of applying the LBT method to power circuits, a simple example is discussed here. Figure 2.1 shows an RL circuit with the square wave input which is a periodic and discontinuous function. The steady state response of this circuit can not be easily found by conventional analysis methods. The proposed LBT is used to find the response in following steps.

Step 1: System ODE is obtained as:

$$L\frac{di}{dt} + Ri(t) = v_{in}(t). \tag{2.19}$$

Step 2: If the input's amplitude and period are denoted by A and T, then $V_{in}(s)$ is derived as:

$$V_{in}(s) = \frac{A(1 - e^{-0.5Ts})}{s(1 + e^{-0.5Ts})} \tag{2.20}$$

Step 3: Assuming $i(0) = I_0$, the Laplace transform of the ODE results in:

$$(Ls + R)I(s) - LI_0 = V_{in}(s). \tag{2.21}$$

Step 4: The only root of characteristic equation is $s_j = -R/L$, then I_0 is found by solving the $V_{in}(s_j = -R/L) = LI_0$ as:

$$I_0 = \left(\frac{A}{R}\right)\frac{1 - e^{\frac{TR}{2L}}}{1 + e^{\frac{TR}{2L}}}. \tag{2.22}$$

Step 5: Now if the ODE is solved for only one cycle, periodic solution is obtained.

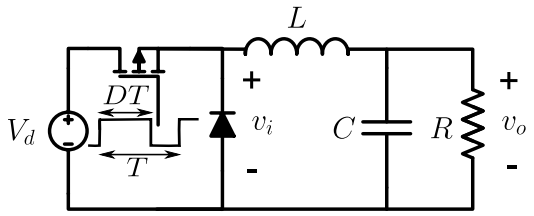

FIGURE 2.3: Schematic of the Buck converter.

Since the input is half-wave symmetrical then the output would be half-wave symmetrical as well and only half cycle of the solution is enough to describe the system response. Thus $L\frac{di}{dt} + Ri(t) = A$ is solved using (2.22):

$$i(t) = \frac{A}{R}\left(1 - \frac{2e^{\frac{TR}{2L}}}{1+e^{\frac{TR}{2L}}}e^{-\frac{R}{L}t}\right) \quad 0 \leq t < \frac{T}{2} \tag{2.23}$$

Figure 2.2 shows steady state voltage across R obtained by (2.23).

2.4 Buck Converter Example

Buck converter is another example that can be analyzed using the LBT method. The converter is shown in Fig. 2.3, where switches are considered ideal. The analysis steps are described as below:

Step 1: Converter ODE is:

$$LC\ddot{v}_o(t) + \frac{L}{R}\dot{v}_o(t) + v_o(t) = v_i(t). \tag{2.24}$$

Step 2: The Laplace transform of the input function is derived as follows, where D is duty ratio and T is switching period:

$$V_i(s) = V_d \frac{1 - e^{-sDT}}{s\left(1 - e^{-sT}\right)}. \tag{2.25}$$

Step 3: If the initial conditions are $v_o(0) = V_0$, $\dot{v}_o(0) = V_0'$ then $G(s)$ is found as:

$$G(s) = \left(LC(sV_0 + V_0') + \frac{L}{R} V_0 \right). \tag{2.26}$$

As the system has a second order ODE, its characteristic equation may have either a pair of complex conjugate poles or two real poles. Therefore, the step 4 is described in two parts:

Step 4A: If $\frac{\sqrt{L/C}}{R} \geq 2$, then characteristic equation has two real poles as below:

$$S_1 = \tfrac{1}{2RC}\left(-1 + \sqrt{1 - 4\tfrac{R^2C}{L}}\right), \quad S_2 = \tfrac{1}{2RC}\left(-1 - \sqrt{1 - 4\tfrac{R^2C}{L}}\right). \tag{2.27}$$

V_0 and V_0' are obtained from $G(s_1) = -V_i(s_1)$, and $G(s_2) = -V_i(s_2)$ as follows:

$$\begin{aligned} V_0 &= \tfrac{V_d}{S_1 - S_2}\left(S_1\left(\tfrac{1-e^{-S_2DT}}{1-e^{-S_2T}}\right) - S_2\left(\tfrac{1-e^{-S_1DT}}{1-e^{-S_1T}}\right)\right) \\ V_0' &= \tfrac{V_d}{(LC)(S_1 - S_2)}\left(\tfrac{1-e^{-S_2DT}}{1-e^{-S_2T}} - \tfrac{1-e^{-S_1DT}}{1-e^{-S_1T}}\right) \end{aligned} \tag{2.28}$$

Now the steady state response could be obtained by solving the ODE for one cycle. With V_0 and V_0' as above, $LC\ddot{v}_o(t) + \frac{L}{R}\dot{v}_o(t) + v_o(t) = V_d$ is solved for $0 \leq t \leq DT$. As characteristic equation has two real poles of S_1 and S_2 the system response would

be as follows:

$$v_o(t) = Ae^{S_1 t} + Be^{S_2 t} + V_d \quad \text{if} \quad 0 \leq t \leq DT \tag{2.29}$$

By substituting steady state initial conditions in (2.29), A and B could be derived as:

$$A = -\frac{S_2(V_0 - V_d) + V_0'}{S_1 - S_2}, B = \frac{S_1(V_0 - V_d) + V_0'}{S_1 - S_2}. \tag{2.30}$$

Since the input function is changed from V_d to zero at $t = DT$, it can be stated that a step function with amplitude of $-V_d$ is added to the system input function at $t = DT$. Therefore, system's zero state response to the mentioned step function has to be obtained and added to (2.29) to find the system response for $DT \leq t \leq T$. System Unit Step Response is obtained as:

$$USR(t) = -\left(\frac{S_2}{S_2 - S_1}e^{S_1 t} - \frac{S_1}{S_2 - S_1}e^{S_2 t} - 1\right). \tag{2.31}$$

For $DT \leq t \leq T$, $v_o(t)$ is:

$$v_o(t) = -V_d \times USR(t - DT) + Ae^{S_1 t} + Be^{S_2 t} + V_d. \tag{2.32}$$

Substituting for $USR(t)$ form (2.31) in (2.32) results in:

$$v_o(t) = \left(A + V_d \frac{S_2}{S_2 - S_1}e^{-S_1 DT}\right)e^{S_1 t} + \left(B - V_d \frac{S_1}{S_2 - S_1}e^{-S_2 DT}\right)e^{S_2 t} \quad \text{if} \quad DT \leq t \leq T. \tag{2.33}$$

Step 4B: If $\frac{\sqrt{L/C}}{R} \leq 2$, then characteristic equation has a pair of complex conjugate poles as below:

$$S_{1,2} = \frac{1}{2RC}\left(-1 \pm j\sqrt{4\frac{R^2 C}{L} - 1}\right) = S_r \pm jS_m. \tag{2.34}$$

Solving $G(S_1) = -V_i(S_1)$, and $G(S_2) = -V_i(S_2)$ results in (2.28). Substituting for S_1 and S_2 from (2.34) in (2.28), V_0 and V_0' are derived as:

$$V_0 = V_d \left[\frac{1-e^{-S_r T}\left(\cos(S_m T) - \frac{S_r}{S_m}\sin(S_m T)\right)}{1+e^{-2S_r T}-2e^{-S_r T}\cos(S_m T)} - \frac{e^{-S_r DT}\left(\cos(S_m DT) + \frac{S_r}{S_m}\sin(S_m DT)\right)}{1+e^{-2S_r T}-2e^{-S_r T}\cos(S_m T)} + \frac{e^{-S_r (1+D)T}\left(\cos(S_m (1-D)T) - \frac{S_r}{S_m}\sin(S_m (1-D)T)\right)}{1+e^{-2S_r T}-2e^{-S_r T}\cos(S_m T)} \right] \tag{2.35}$$

$$V_0' = \frac{V_d}{LCS_m} \frac{e^{-S_r T}\sin(S_m T) - e^{-S_r DT}\sin(S_m DT) - e^{-S_r (1+D)T}\sin(S_m (1-D)T)}{1+e^{-2S_r T}-2e^{-S_r T}\cos(S_m T)}$$

It is worth mentioning that the same result would be obtained by equating the real and imaginary parts of $G(S_1) = -V_i(S_1)$.

With obtained steady initial conditions $LC\ddot{v}_o(t) + \frac{L}{R}\dot{v}_o(t) + v_o(t) = V_d$ is solved for $0 \leq t \leq DT$. As poles are complex conjugate, $v_o(t)$ would be of the form:

$$v_o(t) = e^{S_r t}\left(A\sin\left(S_m t\right) + B\cos\left(S_m t\right)\right) + V_d. \tag{2.36}$$

Again for this case, by substituting the steady state initial conditions, parameters A and B are obtained as below:

$$A = \frac{S_r V_d - S_r V_0 + V_0'}{S_m}, B = V_0 - V_d. \tag{2.37}$$

The Unit Step Response is obtained as:

$$USR(t) = e^{S_r t}\left(\frac{S_r}{S_m}\sin(S_m t) - \cos(S_m t)\right) + 1. \tag{2.38}$$

For $DT \leq t \leq T$, $v_o(t)$ is:

$$v_o(t) = -V_d \times USR(t - DT) + e^{S_r t}\left(A\sin\left(S_m t\right) + B\cos\left(S_m t\right)\right) + V_d. \tag{2.39}$$

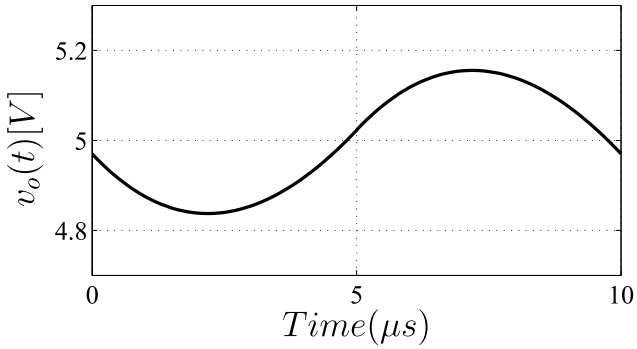

FIGURE 2.4: Output voltage in a Buck converter obtained using the proposed method.

Substituting for $USR(t)$ form (2.38) in (2.39) results in:

$$v_o(t) = e^{S_r t}\left[\left(A + e^{-S_r DT}\left(\frac{S_r}{S_m}\cos(S_m DT) - sin(S_m DT)\right)\right)\sin(S_m t) + \left(B - e^{-S_r DT}\left(\frac{S_r}{S_m}\sin(S_m DT) + cos(S_m DT)\right)\right)\cos(S_m t)\right] \tag{2.40}$$

As an example $v_o(t)$ for the $(V_d = 10V, D = 0.5, L = 10\mu H, C = 10\mu F, f_s = 100kHz, R = 1\Omega)$ is obtained. The characteristic equation has a pair of complex conjugate poles: $S_{1,2} = -50000 \pm j86602$. Using (2.35), $v = 4.97$ and $v' = -6.28 \times 10^5$ are obtained which result in $A = -4.35$ and $B = -5.03$. Therefore, $v_o(t)$ is obtained as:

$$v_0(t) = \begin{cases} -e^{-50000t}\left(4.35\sin(86602t) + 5.03\cos(86602t)\right) + 10 & \text{if } 0 \le t \le DT \\ e^{-50000t}\left(4.35\sin(86602t) + 5.03\cos(86602t)\right) & \text{if } DT \le t \le T \end{cases} \tag{2.41}$$

Figure 2.4 is the plot of (2.41) to better show the ripple part of $v_o(t)$.

2.5 Summary

In this chapter a new mathematical theorem is proposed that finds the steady state initial conditions of an ODE by solving a set of linear equations. As the Laplace transform of an ODE reflects the effects of both input function and initial conditions, the proposed theorem uses the Laplace transform to find the set of initial conditions that compensates the transient response completely. Since the proposed theorem uses Laplace transform that can handle the input function discontinuities, the theorem is adopted to propose a novel analysis for power converters where ODE with discontinuous input is inevitable. The procedure of converter analysis using the proposed method is presented along with simple RL circuit and Buck converter examples. In the following chapters the proposed procedure will be used to analyze more complicated converters with ideal and non ideal waveforms.

Chapter 3

Series Resonant Converter Analysis

In this chapter the LBT approach is applied to a variable duty cycle full bridge Series Resonant Converter (SRC) and the results are validated by simulations and experiments. It is worth mentioning that the LBT method with the procedure presented here could be used to analyze the high order converters like LLC and LCC. Also, LBT could be applied even if the parasitic resistances are included in the model. For the sake of clear illustration a simple SRC with no parasitic resistance is analyzed here to illustrate the method and have a better comparison with the existing literature.

Figure 3.1 shows the SRC converter and its simplified equivalent circuit. As shown in Fig. 3.2 this converter is controlled using phase-shift PWM or variable duty cycle scheme where d is the duty ratio that varies from 0 to 50%, and $d' = 0.5 - d$. Depending on the circuit parameters, at small duty ratios, SRC may enter Discontinuous Conduction Mode (DCM) or it may remain in Continuous Conduction Mode (CCM).

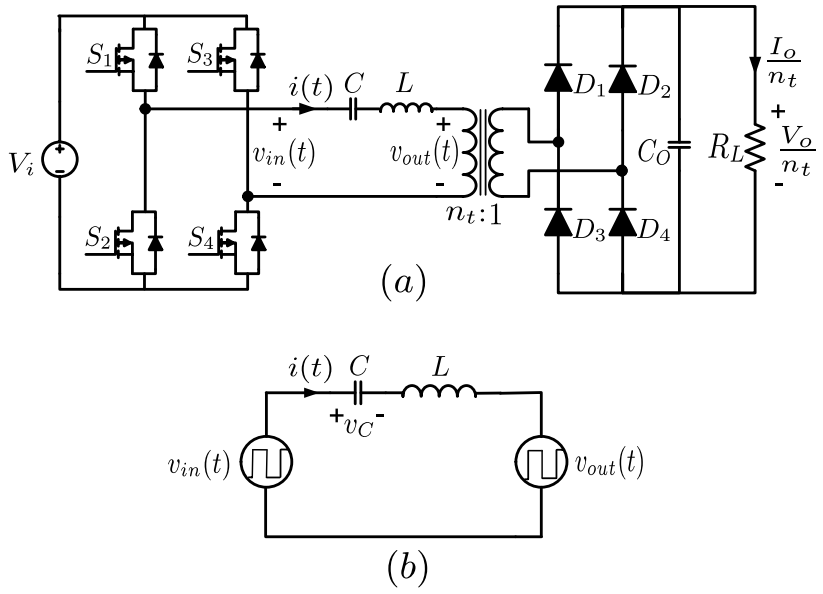

FIGURE 3.1: (a) Schematic of the SRC, and (b) equivalent circuit.

First, it is assumed that SRC remains in CCM mode and all the governing equations are obtained. Then, based on the CCM equations, DCM criteria is derived.

3.1 CCM Operation

The SRC operating under CCM can be modeled by the following differential equation:

$$L\frac{di(t)}{dt} = v_{in}(t) - v_c(t) - v_{out}(t). \tag{3.1}$$

Where $v_{out}(t) = V_o sgn(i(t))$. The sign function appears due to the diode rectifier at the output, because when D_1 and D_4 are turned on the primary side voltage is $+V_o$ and when D_2 and D_3 are turned on then the primary voltage is $-V_o$. According to the Fig. 3.2, inverter output voltage $v_{in}(t)$ could have three levels of V_i, 0, and $-V_i$. The phase shift PWM is used for the inverter and thus $v_{in}(t)$ is symmetrical.

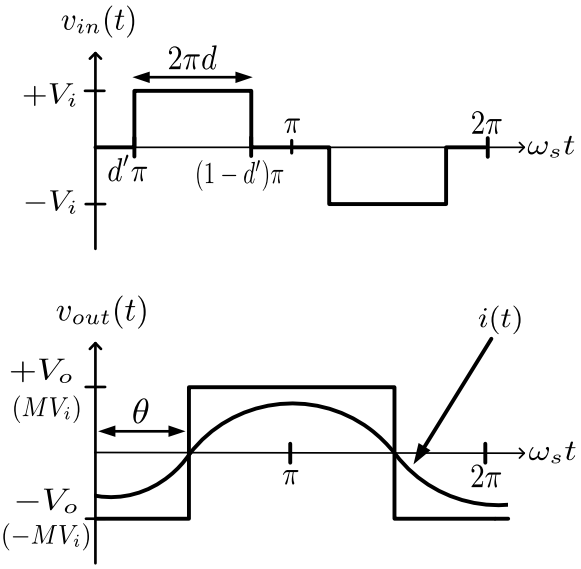

FIGURE 3.2: Typical waveforms of SRC (CCM operation).

$v_{out}(t)$ could only have two levels of $+V_o$ and $-V_o$ depending on the current. When the current is positive $v_{out}(t)$ is positive and vice versa. As $sgn()$ function is nonlinear and $v_{in}(t)$ is discontinuous periodic switching input function, (3.1) is a nonlinear and discontinuous differential equation. Conventionally, this equation was solved either by Fourier series or by tedious stepwise period by period solution to achieve the steady state response. In this paper firstly the non-linearity of the equation is addressed by defining intermediate variables, then the proposed LBT method is used to analyze the converter.

To provide a better insight into the converter characteristics, a normalization is done with the following base values:

$$V_B = V_i, \quad Z_B = n_t^2 R_L. \tag{3.2}$$

Therefore, converter voltage gain is obtained as:

$$M = \frac{V_o}{V_i} \tag{3.3}$$

Also, normalized switching frequency (F) and load quality factor (Q) are defined as:

$$F = \frac{f_s}{f_r} = \frac{\omega_s}{\omega_r}. \tag{3.4}$$

$$Q = \frac{Z_0}{n_t^2 R_L}. \tag{3.5}$$

Where, $\omega_r = \frac{1}{\sqrt{LC}}$ and $Z_0 = \sqrt{\frac{L}{C}}$ are the resonant frequency and characteristic impedance of the resonant tank and $f_s = \frac{\omega_s}{2\pi}$ is the switching frequency. Analysis steps are described as below.

Step 1: Basically, for a given set of F, Q, and d, SRC normalized current and voltage waveforms and accordingly all its characteristics could be obtained. In fact, F, Q, and d are the main variables that are sufficient to describe the SRC behavior. However, two intermediate variables are considered to change the nonlinear differential equation of (3.1) into linear ODE for which LBT could be applied. The non-linearity of (3.1) is due to the presence of $v_{out}(t) = V_o sgn(i(t))$. As it can be seen in Fig. 3.2, if two intermediate variables θ and M are defined, then $v_{out}(t)$ could be described in terms of these variables rather than $V_o sgn\,(i(t))$, and therefore the differential equation won't be nonlinear anymore. θ is the current's phase lag with respect to the input voltage, and M is the voltage gain. At this step two intermediate variables of M and θ are defined such that LBT could be applied to the ODE. Therefore, LBT is applied to obtain the SRC exact equations in terms of M and θ. Then using the obtained equations M and θ are found in terms of F, Q, and d.

Step 2: In order to obtain the system ODE, $i = C\frac{dv_c(t)}{dt}$ is substituted in (3.1):

$$LC\ddot{v}_c(t) + v_c(t) = v_{in}(t) - v_{out}(t). \tag{3.6}$$

Since input function is composed of $v_{in}(t)$ and $-v_{out}(t)$, superposition is used to analyze the ODE. Characteristic equation has a pair of complex conjugate poles as:

$$S_{1,2} = \pm j\frac{1}{\sqrt{LC}} = \pm j\omega_r. \tag{3.7}$$

Step 3: If $v_c(0) = V_0$ and $\dot{v}_c(t) = V_0'$ are considered, then $G(s)$ is obtained as:

$$G(s) = LC\left(sV_0 - V_0'\right). \tag{3.8}$$

Step 4: Laplace transform of each input function is obtained as below:

$$F_1(s) = \mathcal{L}\left\{v_{in}(t)\right\} = \frac{\int_0^{\frac{\pi}{\omega_s}} e^{-st}v_{in}(t)dt}{1 + e^{-s\frac{\pi}{\omega_s}}} = \frac{V_i}{s}\frac{e^{-sd'\pi}\left(1 - e^{-s2\pi d}\right)}{1 + e^{-s\frac{\pi}{\omega_s}}}. \tag{3.9}$$

$$F_2(s) = \mathcal{L}\left\{-v_{out}(t)\right\} = \frac{\int_0^{\frac{\pi}{\omega_s}} -e^{-st}v_{out}(t)dt}{1 + e^{-s\frac{\pi}{\omega_s}}} = \frac{MV_i}{s}\left(1 - \frac{2e^{-s\frac{\theta}{\omega_s}}}{1 + e^{-s\frac{\pi}{\omega_s}}}\right). \tag{3.10}$$

Step 5: Equating the real and imaginary parts of $G(s = j\omega_r) = -F_1(s = j\omega_r)$ results in:

$$\begin{aligned} V_0 &= 0 \\ V_0' &= -V_i\omega_r\frac{\sin\left(\frac{\pi d}{F}\right)}{\cos\left(\frac{\pi}{2F}\right)}. \end{aligned} \tag{3.11}$$

Now $LC\ddot{v}_c(t) + v_c(t) = v_{in}(t)$ has to be solved to obtain the first part of solution. Due to half-wave symmetry, only half cycle of the solution is enough to describe it. $LC\ddot{v}_c(t) + v_c(t) = 0$ with obtained V_0 and V_0' is solved for $0 \leq \omega_s t \leq d'\pi$ that results

in:

$$v_c(t) = -V_i \frac{\sin\left(\frac{\pi d}{F}\right)}{\cos\left(\frac{\pi}{2F}\right)} \sin(\omega_r t). \tag{3.12}$$

In order to obtain the solution for the rest of the period, Unit Step Response is obtained as:

$$USR(t) = 1 - \cos(\omega_r t). \tag{3.13}$$

As it can be seen in Fig. 3.2, v_{in} is added by V_i at $\omega_s t = d'\pi$ and again it is subtracted by $-V_i$ at $\omega_s t = (1-d')\pi$. Therefore, first part of $v_c(t)$ is obtained as:

$$v_{c1}(t) = \begin{cases} -V_i \frac{\sin\left(\frac{\pi d}{F}\right)}{\cos\left(\frac{\pi}{2F}\right)} \sin(\omega_r t) & \text{if } \ 0 \le \omega_s t \le d'\pi \\ -V_i \frac{\sin\left(\frac{\pi d}{F}\right)}{\cos\left(\frac{\pi}{2F}\right)} \sin(\omega_r t) + V_i \left(1 - \cos(\omega_r t - \frac{d'\pi}{F})\right) & \text{if } \ d'\pi \le \omega_s t \le (1-d')\pi \\ V_i \frac{\sin\left(\frac{\pi d}{F}\right)}{\cos\left(\frac{\pi}{2F}\right)} \sin(\omega_r t - \frac{\pi}{F}) & \text{if } \ (1-d')\pi \le \omega_s t \le \pi \end{cases} \tag{3.14}$$

Step 6: In this step second part of the solution that is caused by $v_{out}(t)$ is obtained. V_0 and V_0' are obtained by equating the real and imaginary parts of $G(s = j\omega_r) = -F_2(s = j\omega_r)$ as:

$$\begin{aligned} V_0 &= MV_i \left(1 - \frac{\cos\left(\frac{\pi}{2F} - \frac{\theta}{F}\right)}{\cos\left(\frac{\pi}{2F}\right)}\right) \\ V_0' &= MV_i\omega_r \frac{\sin\left(\frac{\pi}{2F} - \frac{\theta}{F}\right)}{\cos\left(\frac{\pi}{2F}\right)} \end{aligned} \tag{3.15}$$

Now $LC\ddot{v}_c(t) + v_c(t) = -v_{out}(t)$ has to be solved. $LC\ddot{v}_c(t) + v_c(t) = MV_i$ with obtained V_0 and V_0' is solved for $0 \le \omega_s t \le d'\pi$ that results in:

$$v_c(t) = MV_i \left(1 + \frac{\sin\left(\frac{\pi}{2F} - \frac{\theta}{F}\right)}{\cos\left(\frac{\pi}{2F}\right)} \sin(\omega_r t) - \frac{\cos\left(\frac{\pi}{2F} - \frac{\theta}{F}\right)}{\cos\left(\frac{\pi}{2F}\right)} \cos(\omega_r t)\right). \tag{3.16}$$

This equation could be further simplified to:

$$v_c(t) = MV_i \left[1 + \tan\left(\frac{\pi}{2F}\right) \sin\left(\omega_r t - \frac{\theta}{F}\right) - \cos\left(\omega_r t - \frac{\theta}{F}\right) \right] \tag{3.17}$$

System $USR(t)$ is obtained in previous step, and it is sufficient to sum $-2MV_i \times USR(t - \frac{\theta}{F\omega_r})$ with obtained $v_c(t)$ to derive the solution for $\theta \leq \omega_s t \leq \pi$.

$$v_{c2}(t) = \begin{cases} MV_i \left[1 + \tan\left(\frac{\pi}{2F}\right) \sin\left(\omega_r t - \frac{\theta}{F}\right) - \cos\left(\omega_r t - \frac{\theta}{F}\right) \right] & \text{if } \ 0 \leq \omega_s t \leq \theta \\ MV_i \left[-1 + \tan\left(\frac{\pi}{2F}\right) \sin\left(\omega_r t - \frac{\theta}{F}\right) + \cos\left(\omega_r t - \frac{\theta}{F}\right) \right] & \text{if } \ \theta \leq \omega_s t \leq \pi \end{cases} \tag{3.18}$$

according to the superposition theorem, $v_c(t)$ is the sum of $v_{c1}(t)$ and $v_{c2}(t)$. Since θ may be either greater or less than $d'\pi$, two possible waveforms for $v_c(t)$ is obtained as below.

$$\text{if } \ d'\pi < \theta \quad v_c(t) = \begin{cases} v_{c1}(t) + v_{c3}(t) & 0 \leq \omega_s t < d'\pi \\ v_{c2}(t) + v_{c3}(t) & d'\pi \leq \omega_s t < \theta \\ v_{c2}(t) + v_{c4}(t) & \theta \leq \omega_s t < (1-d')\pi \\ -v_{c1}(t - \frac{\pi}{F\omega_r}) + v_{c4}(t) & (1-d')\pi \leq \omega_s t < \pi \end{cases} \tag{3.19}$$

$$\text{if } \ d'\pi \geq \theta \quad v_c(t) = \begin{cases} v_{c1}(t) + v_{c3}(t) & 0 \leq \omega_s t < \theta \\ v_{c1}(t) + v_{c4}(t) & \theta \leq \omega_s t < d'\pi \\ v_{c2}(t) + v_{c4}(t) & d'\pi \leq \omega_s t < (1-d')\pi \\ -v_{c1}(t - \frac{\pi}{F\omega_r}) + v_{c4}(t) & (1-d')\pi \leq \omega_s t < \pi \end{cases} \tag{3.20}$$

$$
\begin{aligned}
v_{c1}(t) &= -V_i \frac{\sin\left(\frac{\pi d}{F}\right)}{\cos\left(\frac{\pi}{2F}\right)} \sin(\omega_r t) \\
v_{c2}(t) &= -V_i \frac{\sin\left(\frac{\pi d}{F}\right)}{\cos\left(\frac{\pi}{2F}\right)} \sin(\omega_r t) + V_i \left(1 - \cos(\omega_r t - \tfrac{d'\pi}{F})\right) \\
v_{c3}(t) &= MV_i \left[1 + \tan\left(\tfrac{\pi}{2F}\right) \sin\left(\omega_r t - \tfrac{\theta}{F}\right) - \cos\left(\omega_r t - \tfrac{\theta}{F}\right)\right] \\
v_{c4}(t) &= MV_i \left[-1 + \tan\left(\tfrac{\pi}{2F}\right) \sin\left(\omega_r t - \tfrac{\theta}{F}\right) + \cos\left(\omega_r t - \tfrac{\theta}{F}\right)\right]
\end{aligned}
$$

Current equations ($i(t)$) can be found by differentiation of the (3.19) and (3.20). As shown in Fig. 3.2, if $d'\pi < \theta$, then SRC has Zero Voltage Switching (ZVS) and corresponding current waveform is derived as (3.21), and if $d'\pi \geq \theta$, then ZVS is lost and corresponding current waveform is derived as (3.22).

$$
\text{if } \; d'\pi < \theta \quad i(t) = \begin{cases} i_1(t) + i_3(t) & 0 \leq \omega_s t < d'\pi \\ i_2(t) + i_3(t) & d'\pi \leq \omega_s t < \theta \\ i_2(t) + i_4(t) & \theta \leq \omega_s t < (1-d')\pi \\ -i_1(t - \frac{\pi}{F\omega_r}) + i_4(t) & (1-d')\pi \leq \omega_s t < \pi \end{cases} \tag{3.21}
$$

$$
\text{if } \; d'\pi \geq \theta \quad i(t) = \begin{cases} i_1(t) + i_3(t) & 0 \leq \omega_s t < \theta \\ i_1(t) + i_4(t) & \theta \leq \omega_s t < d'\pi \\ i_2(t) + i_4(t) & d'\pi \leq \omega_s t < (1-d')\pi \\ -i_1(t - \frac{\pi}{F\omega_r}) + i_4(t) & (1-d')\pi \leq \omega_s t < \pi \end{cases} \tag{3.22}
$$

$$
\begin{aligned}
i_1(t) &= -V_i C\omega_r \frac{\sin\frac{\pi d}{F}}{\cos\frac{\pi}{2F}} \cos(\omega_r t) \\
i_2(t) &= V_i C\omega_r \left(-\frac{\sin\frac{\pi d}{F}}{\cos\frac{\pi}{2F}} \cos(\omega_r t) + \sin(\omega_r t - \tfrac{d'\pi}{F})\right) \\
i_3(t) &= MV_i C\omega_r \left(\tan\tfrac{\pi}{2F} \cos(\omega_r t - \tfrac{\theta}{F}) + \sin(\omega_r t - \tfrac{\theta}{F})\right) \\
i_4(t) &= MV_i C\omega_r \left(\tan\tfrac{\pi}{2F} \cos(\omega_r t - \tfrac{\theta}{F}) - \sin(\omega_r t - \tfrac{\theta}{F})\right)
\end{aligned}
$$

Step 7: Using the LBT all of the SRC closed form equations at steady state are obtained in terms of intermediate variables M and θ. At this step using the closed form equations, M and θ will be derived in terms of main variables F, Q, and d. As shown in Fig. 3.2, the current at $\omega_s t = \theta$ is zero, and $i(\theta) = 0$ is one of the equations that are formed to find θ and M. The other equation is formed by calculating the converter voltage gain based on obtained current waveform. The substitution method is used to find two variables M and θ from two mentioned equations. For the first equation, if $d'\pi < \theta$, then $i(\omega_s t = \theta) = i_2\left(\frac{\theta}{F\omega_r}\right) + i_3\left(\frac{\theta}{F\omega_r}\right) = 0$ has to be solved, and if $d'\pi \geq \theta$, then $i(\omega_s t = \theta) = i_1\left(\frac{\theta}{F\omega_r}\right) + i_3\left(\frac{\theta}{F\omega_r}\right) = 0$ has to be solved. Therefore θ is derived as follows:

$$\theta = \begin{cases} \frac{\pi}{2} - F\sin^{-1}\left(M\frac{\sin\frac{\pi}{2F}}{\cos\frac{\pi d'}{F}}\right) & \text{if } \; d'\pi < \theta, \\ F\cos^{-1}\left(M\frac{\sin\frac{\pi}{2F}}{\sin\frac{\pi d}{F}}\right) & \text{if } \; d'\pi \geq \theta \end{cases} \tag{3.23}$$

Now the voltage gain has to be obtained and equation (3.23) has to be plugged into voltage gain equation to find both M and θ in terms of F,Q, and d. In order to find the voltage gain in terms of main variables, V_o should be found in terms of V_i. As shown in Fig. 3.1(a), $V_o = I_o R_L$, where I_o is the DC component of full-wave rectified series current:

$$I_0 = \frac{1}{\pi}\int_{\theta}^{\pi+\theta} i(t)d(\omega_s t). \tag{3.24}$$

Using (3.21) and (3.22), I_0 is calculated as:

$$I_0 = \begin{cases} \frac{V_i}{R_L}\frac{2F}{\pi Q}\left(\frac{\sin\left(\frac{\pi d}{F}\right)}{\cos\left(\frac{\pi}{2F}\right)}\sin\left(\frac{\theta}{F}\right) + \cos\left(\frac{\theta}{F} - \frac{\pi d'}{F}\right) - 1\right) & \text{if } \; d'\pi < \theta, \\ \frac{V_i}{R_L}\frac{2F}{\pi Q}\left(\frac{\sin\left(\frac{\pi d}{F}\right)}{\cos\left(\frac{\pi}{2F}\right)}\sin\left(\frac{\theta}{F}\right)\right) & \text{if } \; d'\pi \geq \theta \end{cases} \tag{3.25}$$

Now, if θ is substituted from (3.23) in (3.25), M can be found in terms of d, F and Q as follows:

$$M = \begin{cases} \left(\frac{2F}{\pi Q}\right) \frac{AB\sqrt{A^2+B^2-1}-B^2}{A^2+B^2} & \text{if } d'\pi < \theta, \\ \left(\frac{2F}{\pi Q}\right) \frac{\sin\left(\frac{\pi d}{F}\right)}{\sqrt{\left(\frac{2F}{\pi Q}\sin\left(\frac{\pi}{2F}\right)\right)^2+\cos^2\left(\frac{\pi}{2F}\right)}} & \text{if } d'\pi \geq \theta, \end{cases} \tag{3.26}$$

$$A = \sin\left(\frac{\pi d}{F}\right)\tan\left(\frac{\pi}{2F}\right) + \cos\left(\frac{\pi d}{F}\right), \quad B = \frac{\pi Q \cos\left(\frac{\pi d'}{F}\right)}{2F\sin\left(\frac{\pi}{2F}\right)}$$

Using (3.23) and (3.26), θ could be calculated in terms of d, F, and Q as:

$$\theta = \begin{cases} \frac{\pi}{2} - F\sin^{-1}\left(\frac{A\sqrt{A^2+B^2-1}-B}{A^2+B^2}\right) & \text{if } \ d'\pi < \theta, \\ F\cos^{-1}\left(\left(1+\left(\frac{\pi Q}{2F}\cot\frac{\pi}{2F}\right)^2\right)^{-\frac{1}{2}}\right) & \text{if } \ d'\pi \geq \theta \end{cases} \tag{3.27}$$

It can be observed from (3.27) that for lower duty ratios where $d'\pi \geq \theta$, the value of θ is not a function of d anymore and it is a constant value if the tank parameters F and Q are constant. There is also a physical interpretation for this observation. The current phase lag (θ), depends on the circuit seen from the inverter terminals ($v_{in}(t)$). In case of $d'\pi < \theta$, (see Fig. 3.2), for $\omega_s t$ in $[d'\pi \quad \theta]$, the inverter terminals absorb power and a negative dc source ($-MV_i$) in series with resonant tank is connected to terminals. However, for $\omega_s t$ in $[\theta \quad (1-d')\pi]$, the inverter terminals inject power and a positive dc source ($+MVi$) in series with resonant tank is connected to terminals. The overall circuit seen from inverter terminals depends on the relative duration of these intervals. By changing duty cycle the relative duration of these intervals is changed and consequently θ is changed. However, in case of $d'\pi \geq \theta$, (see Fig. 3.3) regardless of duty cycle the inverter terminals always inject power and a positive dc

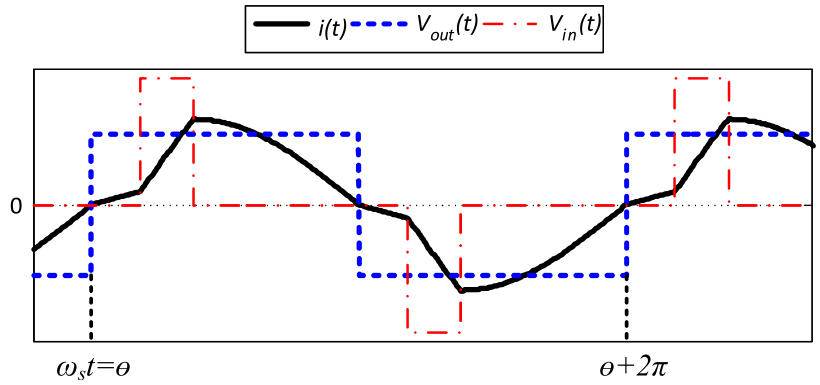

FIGURE 3.3: Current waveform if converter remains in CCM for $d < d_{ZVS}$ (No ZVS).

source ($+MVi$) in series with resonant tank is connected to terminals. Thus, the circuit seen from inverter terminals and consequently θ are independent of duty cycle and only depend on F and Q. Therefore, for any F and Q there exists a critical duty ratio d_{ZVS} where for all duty cycles smaller than that, θ is equal to the constant value as expressed in (3.27).

$$d_{ZVS} = 0.5 - \frac{F}{\pi}\cos^{-1}\left(\left(1+\left(\frac{\pi Q}{2F}\cot\frac{\pi}{2F}\right)^2\right)^{-\frac{1}{2}}\right) \tag{3.28}$$

In fact if $d > d_{ZVS}$, then $d'\pi < \theta$ and converter is in ZVS mode and if $d < d_{ZVS}$, then $d'\pi \geq \theta$ and ZVS is lost. Therefore, equations 3.21-3.27 can be rewritten using two conditions of $d > d_{ZVS}$ and $d \leq d_{ZVS}$ to become independent of θ. The $sgn()$ function in (3.1) can now be eliminated by obtaining d_{ZVS}. Having F and Q, first d_{ZVS} is obtained from (3.28), then θ, M, and $i(t)$ corresponding to each d could be calculated using the above mentioned equations.

When $d > d_{ZVS}$, converter always operates in CCM and (3.21) is the only possible current waveform. But as discussed earlier for low duty ratios where $d \leq d_{ZVS}$

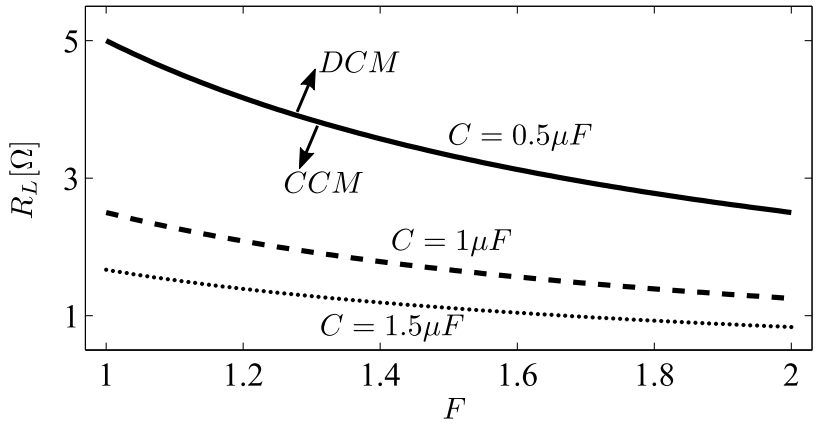

FIGURE 3.4: DCM boundary in $R_L - F$ plane for $f_r = 100kHz$.

converter may stay in CCM where current waveform is derived as (3.22) or it may enter DCM and operate under ZCS. In DCM, (3.1) does not describe its behavior anymore and another ODE that describes the system behavior under DCM should be derived. CCM current waveform can be used to find the boundary condition for the DCM operation. Figure 3.3 shows the CCM operation for $d \leq d_{ZVS}$. It can be observed that, if the slope of current is positive right after $\omega_s t = \theta$ then converter operates at CCM otherwise it has entered DCM. According to (3.22) slope of the current at $\omega_s t = \theta$ is $\dot{i}_1(\theta/\omega_s) + \dot{i}_4(\theta/\omega_s)$ which is non-positive if and only if $\pi Q \leq 2F$. Therefore, the necessary condition for converter to enter DCM is:

$$Q \leq \frac{2}{\pi} F \tag{3.29}$$

It is worth mentioning that the same result has been reported in the previous studies [32, 33].

The obtained boundaries for DCM and ZVS are plotted in Fig. 3.4 and Fig. 3.5 respectively. Figure 3.4 shows the DCM boundary in $R_L - F$ plane for $f_r = 100kHz$ and different values of C. It is observed that by increasing C and F SRC enters

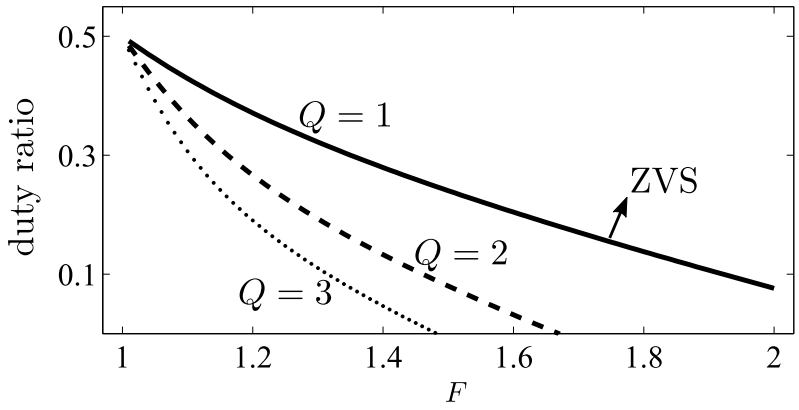

FIGURE 3.5: ZVS boundary (d_{ZVS}) versus F for different Q values.

DCM for smaller R_L values. Also Fig. 3.5 shows the ZVS boundary (d_{ZVS}) versus F for different Q values. It can be seen that by increasing F and Q the ZVS range increases.

According to Fig. 3.4 and Fig. 3.5, the variable dusty ratio SRC may have three operating modes as:

1. Discontinuous Conduction mode.
2. Continuous Conduction Mode with Zero Voltage Switching ($d \geq d_{ZVS}$).
3. Continuous Conduction Mode without Zero Voltage Switching ($d < d_{ZVS}$).

Fig. 3.6 shows the all three possible operating modes for a SRC with $Q = 1$. It can be observed that for lower F values converter always operates in CCM, but ZVS could be lost by reducing d. However, for larger F values converter operates in CCM with ZVS at large duty ratios and by decreasing the duty ratio SRC enters DCM. Also the point in which all three modes meet is so called triple point and it is shown in Fig. 3.6. At triple point, $Q = \frac{\pi}{2}F$, and $d = d_{ZVS}$. If these conditions are plugged

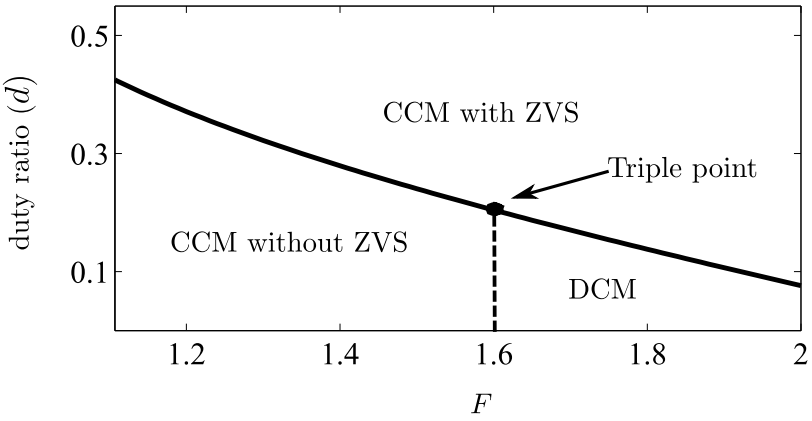

FIGURE 3.6: Three different operating modes for $Q = 1$ in $d - F$ plane.

into (3.28), (3.26) the converter duty ratio at triple point d_{triple} and its gain at triple point M_{triple} could be obtained as:

$$d_{triple} = 1 - \frac{F}{2}. \tag{3.30}$$

$$M_{triple} = \sin\left(\frac{\pi}{F} - \frac{\pi}{2}\right). \tag{3.31}$$

Therefore, converter duty ratio and its gain at ripple point only depend on F value. Figure 3.7 and Fig. 3.8 show the the SRC's triple point duty ratio and gain respectively. It can be concluded that no DCM occurs for $F \geq 2$, because the triple point reaches zero and converter always operates within CCM.

3.2 DCM Analysis

Figure 3.9 shows the DCM operation waveform. Right before $\omega_s t = 0$ resonant tank current is zero but the tank capacitor has an unknown initial voltage $-V_{dcm}$. After applying the positive input voltage, the tank current starts rising and reaches its

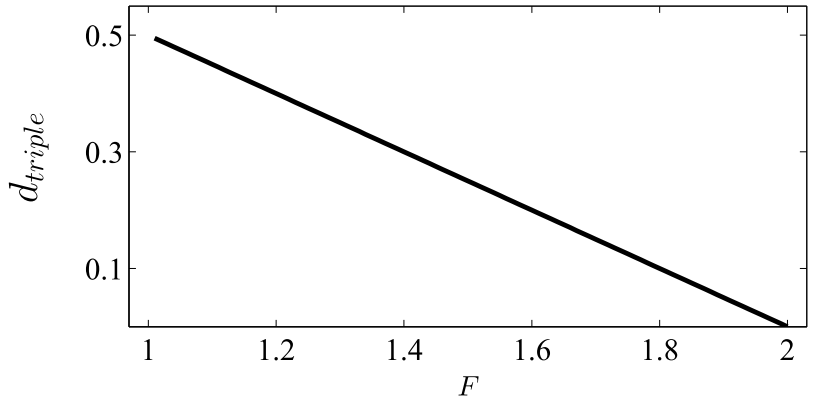

FIGURE 3.7: SRC d_{triple} in $d - F$ plane.

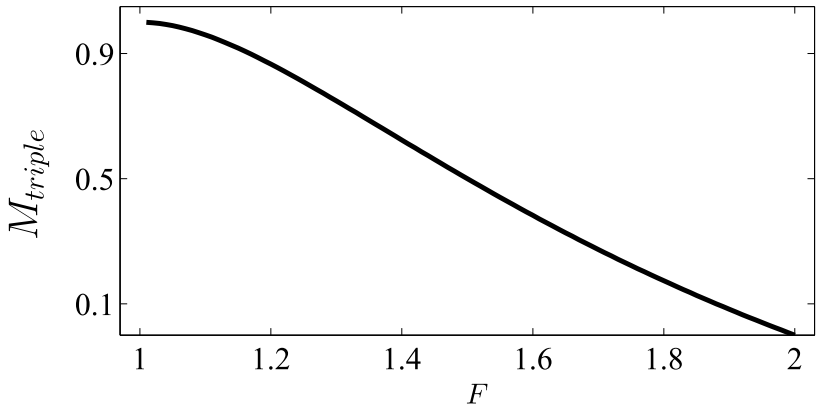

FIGURE 3.8: SRC M_{triple} in $M - F$ plane.

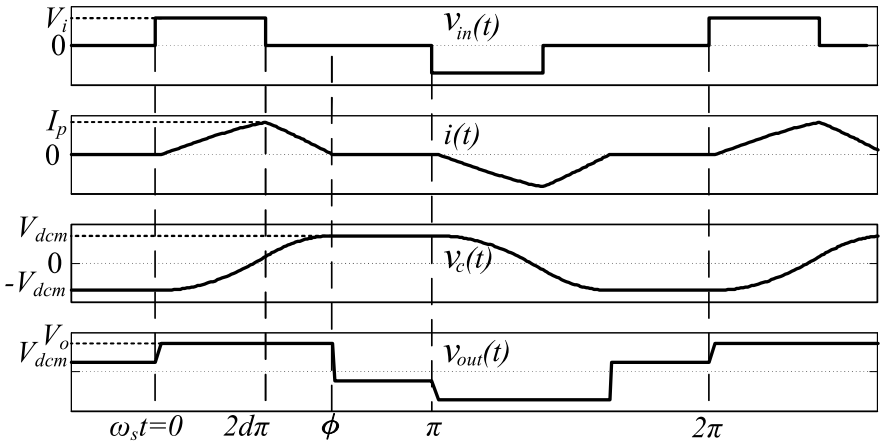

FIGURE 3.9: DCM operation waveform.

peak value at $\omega_s t = 2d\pi$. The capacitor voltage increases as long as the resonant tank current is positive. At $\omega_s t = 2d\pi$ input voltage is switched to zero when the energy stored in the inductor starts discharging into the load and resonant capacitor. At an unknown instant $\omega_s t = \phi$, inductor current reaches zero and remains zero until the next half-cycle. When the current is zero, none of the output diodes conduct and the load is isolated from the resonant circuit. During this period, the primary voltage of the transformer will be equal to the capacitor voltage at $\omega_s t = \phi$ to keep the inductor current equal to zero. In other words, from $\omega_s t = \phi$ to $\omega_s t = \pi$, both capacitor and transformer primary voltages are constant and equal to the capacitor voltage at $\omega_s t = \phi$.

Due to the symmetry, capacitor voltage at $\omega_s t = \pi$ must be equal to V_{dcm}. To analyze the circuit, equivalent circuit of Fig. 3.1(b) is used for $v_{in}(t)$ and $v_{out}(t)$ as shown in Fig. 3.9. In order to find unknown variables V_{dcm} and ϕ, LBT method is used and the steady state initial conditions are obtained in terms of V_{dcm} and ϕ. Since at steady state condition $i(0) = 0$ and $v_c(0) = -V_{dcm}$, two equations are formed from the calculated initial conditions and are solved to determine V_{dcm} and ϕ as follows:

$$\phi = 2F \tan^{-1}\left(\frac{\sin(\frac{2d\pi}{F})}{\cos(\frac{2d\pi}{F}) + 2M - 1}\right) \tag{3.32}$$

$$V_{dcm} = \frac{(M-1)\left(\cos(\frac{2d\pi}{F}) - 1\right)}{\cos(\frac{2d\pi}{F}) + 2M - 1} V_i \tag{3.33}$$

Two variables V_{dcm} and ϕ are sufficient to analyze the converter and find all converter signals. For example, due to the symmetry only half cycle of the current waveform is enough to determine $i(t)$:

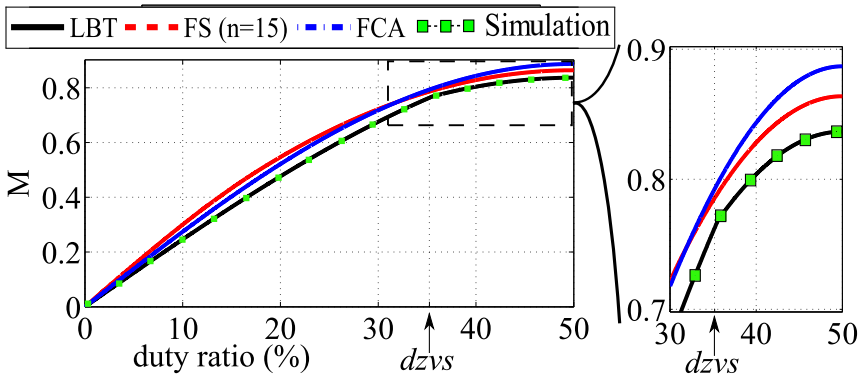

FIGURE 3.10: Comparison of voltage gains calculated using the proposed method and other methods. $Q = 1 \& F = 1.23$

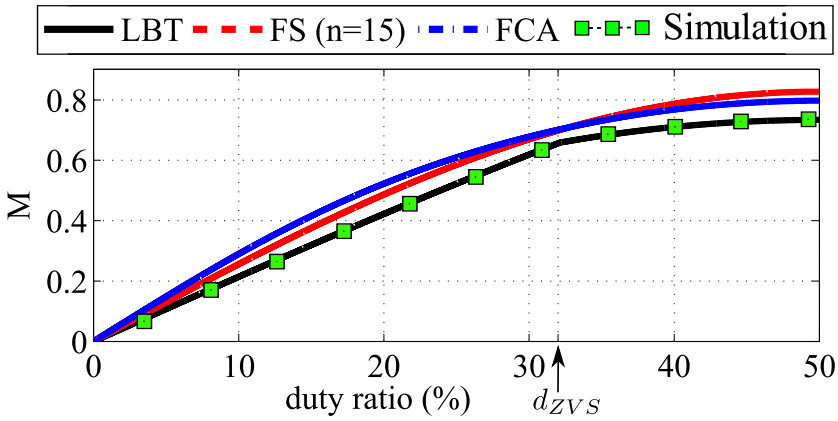

FIGURE 3.11: Comparison of voltage gains calculated using the proposed method and other methods. $Q = 0.4 \& F = 1.9$

$$i(t) = \begin{cases} -V_i C \omega_r \frac{(M-1)(2M)}{\cos(\frac{2\pi d}{F})+2M-1} \sin(\omega_r t) & 0 \le \omega_s t \le 2d\pi \\ -V_i C \omega_r \left[\frac{(M-1)(2M)}{\cos(\frac{2\pi d}{F})+2M-1} \sin(\omega_r t) + \sin(\omega_r t - \frac{2\pi d}{F}) \right] & 2d\pi \le \omega_s t \le \phi \\ 0 & \phi \le \omega_s t \le \pi \end{cases} \quad (3.34)$$

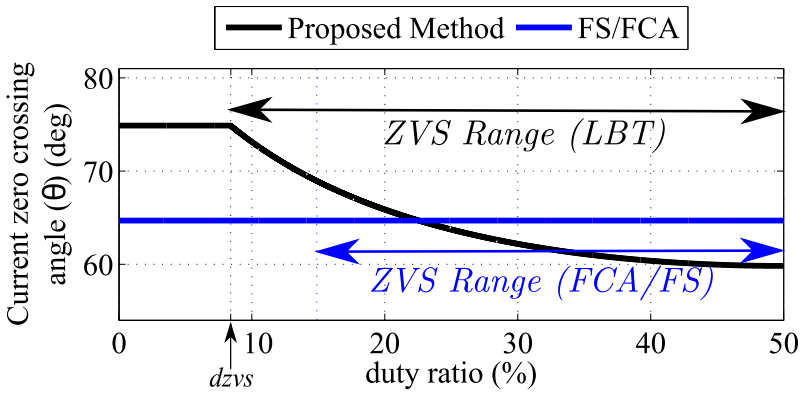

FIGURE 3.12: Current zero crossing point (θ) and ZVS range based on proposed method and other methods. $Q = 2.5 \& F = 1.4$

3.3 Comparison of the Proposed Method with FCA and FS

In this section the results of the analyses are plotted and compared with the FS/FCA. For ($F = 1.23$ & $Q = 1$) that are the parameters of the experimental setup, voltage gain is plotted in terms of duty ratio as shown in Fig. 3.10. It can be seen that for $d = 50\%$ the gain predicted by the proposed method is 0.83. While, the gain predicted by FS and FCA methods (considering 15 harmonics) are 0.86 and 0.88 respectively. Simulation results confirm the prediction of the proposed method. Also, in Fig. 3.11 another comparison is carried out for ($F = 1.9$ & $Q = 0.4$). As for this case load quality factor is low and converter is operating far from resonant frequency the FCA/FS prediction error is relatively large (about 15%).

Figure 3.12 shows the plot of the current zero crossing angle (θ), in terms of duty ratio for ($F = 1.4$ & $Q = 2.5$). Due to the symmetry, FS and FCA methods provide similar results. Although both FS/FCA analysis predict that θ is independent of d, the proposed method shows that θ increases as d decreases. This is especially

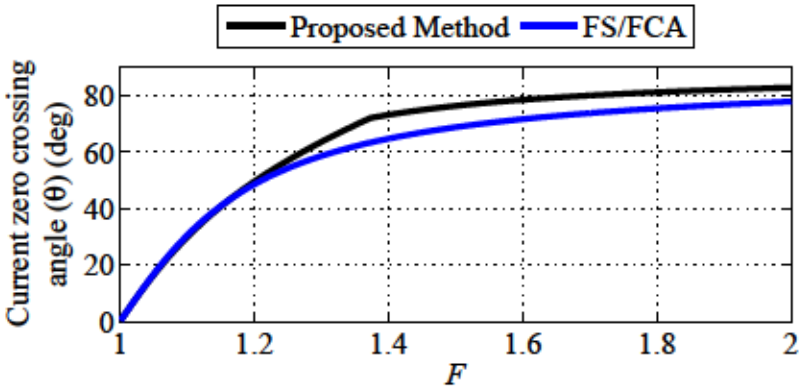

FIGURE 3.13: Current zero crossing point (θ) versus F. $Q = 2.5 \& d = 0.1$

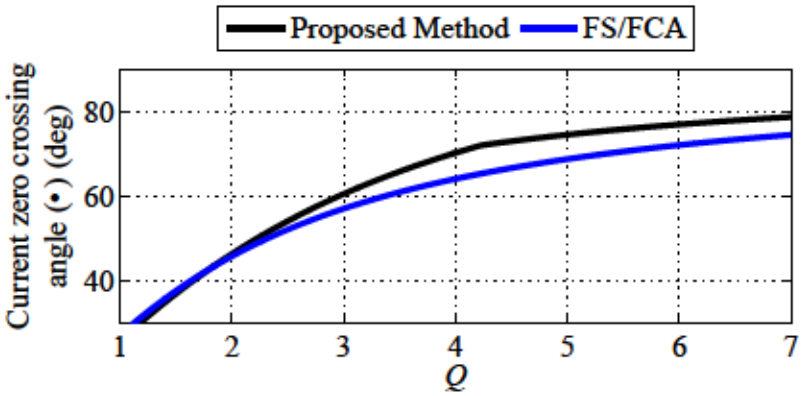

FIGURE 3.14: Current zero crossing point (θ) versus Q. $F = 1.23 \& d = 0.1$

important in the prediction of zero voltage switching (ZVS) of the converter as ZVS directly depends on θ. Therefore, ZVS range calculated by FS/FCA analysis is smaller than the proposed method for this condition and it can be seen that LBT leads to a better design.

Figures 3.13 and 3.14 are sketched for a constant duty cycle ($d = 0.1$). In Fig. 3.13 a constant load ($Q = 2.5$) is assumed. It is shown that for large F values, $d'\pi \geq \theta$ and converter operates with ZVS. However, by reducing the F value, θ decreases until it reaches $d'\pi = 72deg$, when ZVS is lost. According to FS/FCA prediction ZVS is lost at $F = 1.6$, while based on LBT prediction ZVS is lost at $F = 1.37$. According

to Fig. 3.12 the maximum difference in θ prediction by FS/FCA and LBT method occurs at d_{ZVS} where the LBT predicts the ZVS violation. Therefore, it can be seen in Fig. 3.13 that the maximum error in θ prediction is occurred at $F = 1.37$. In Fig. 3.14 a constant F ($F = 1.23$) is assumed. θ is reduced, by reducing the load (Q), until ZVS is lost. FS/FCA predicts $Q = 6$ when ZVS is lost and LBT predicts $Q = 4.2$ when ZVS is lost. Therefore, the maximum error occurs at $Q = 4.2$.

3.4 Simulation and Experimental Results

To validate the proposed method, SRC circuit is experimentally tested. In this setup the parameters are chosen as shown in table 3.1:

Parameter	Value
Resonant inductance L	$5.1\mu H$
Resonant capacitance C	$0.8\mu F$
Transformer ratio $\frac{N_p}{N_s}$	$\frac{1}{24}$
Load resistance R_L	1450Ω
Switching frequency f_s	$97kHz$

TABLE 3.1: Table of experimental setup parameters.

This SRC converter basically boosts up the input dc voltage of Fuel Cell or PV resources. In this design switching frequency and load resistance are chosen as $f = 97kHz$, $R_L = 1450\Omega$ to provide $F = 1.23$, and $Q = 1$. According to Fig. 3.10 it is predicted that this converter can boost a $20V$ input up to 400V output voltage at duty ratio equal to 50% which leads to 110W power transfer. For ($F = 1.23$ & $Q = 1$), Fig. 3.15 shows the $i(pu)$ and $v_{out}(pu)$ waveforms based on different methods and simulated waveforms obtained form PSIM software. It is observed that

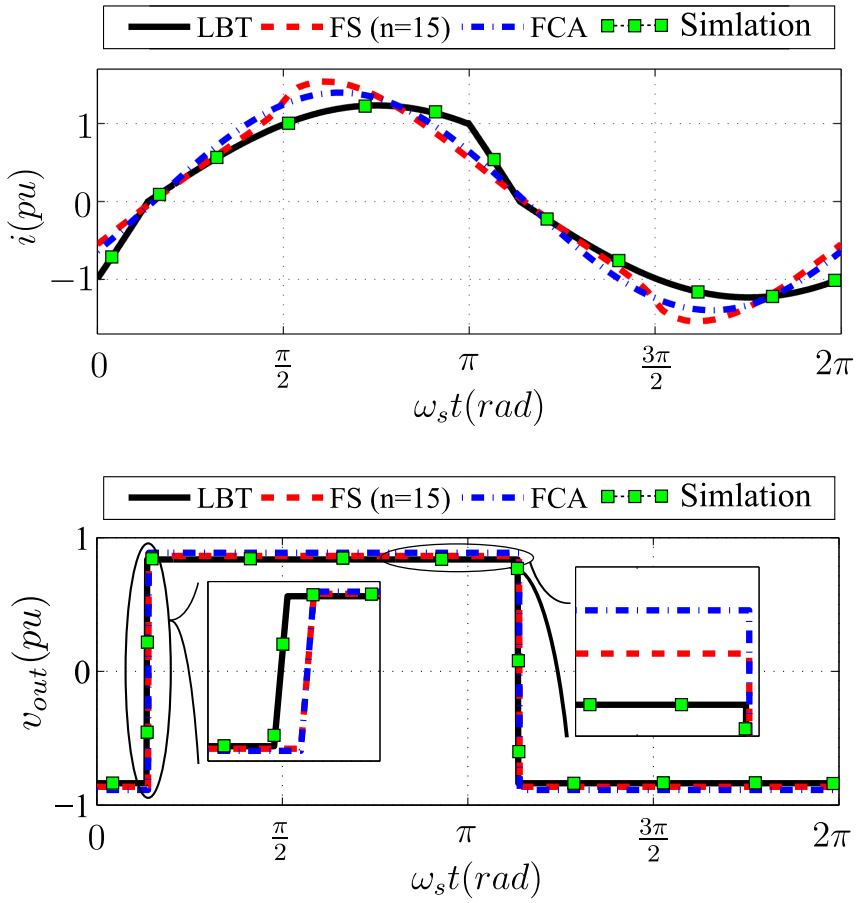

FIGURE 3.15: Calculated $i(pu)$ and $v_{out(pu)}$ waveforms based on LBT method and other methods versus simulation results. $Q = 1 \& F = 1.23$

the plots obtained from the LBT method exactly match the simulation results. Also it is worth mentioning that the calculated voltage gain $M = 0.83$ is validated by this simulation result. This scenario is also experimentally validated and results are shown in Fig. 3.16. It is worth noting that the proposed method calculates the current phase lag as 24.6 degrees (0.43 rad) or 720ns which exactly matches with experimental results in Fig. 3.16.

Moreover, Fig. 3.17 compares the experimental and calculated current waveforms. It

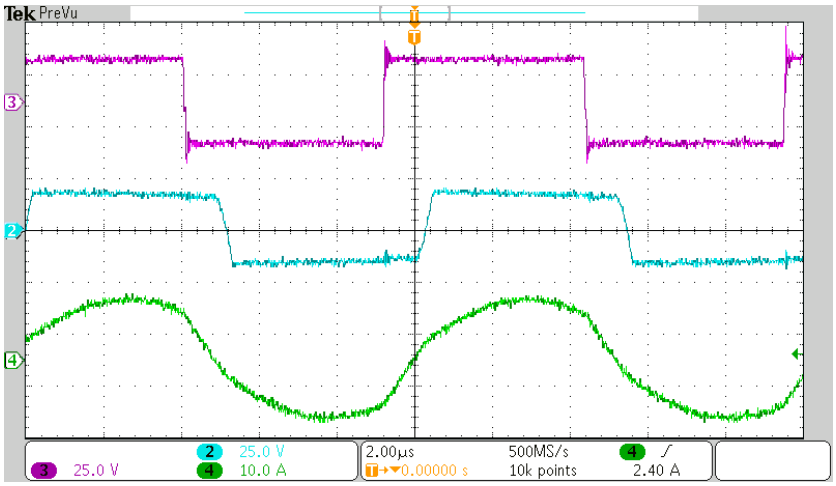

FIGURE 3.16: Experimental results (V_{in} = 20, d = 50%) Ch2: Transformer primary voltage (V_{out}) with 25V/div. Ch3: Inverter voltage (V_{in}) with 25V/div. Ch4: Series current (i) with 10A/div.

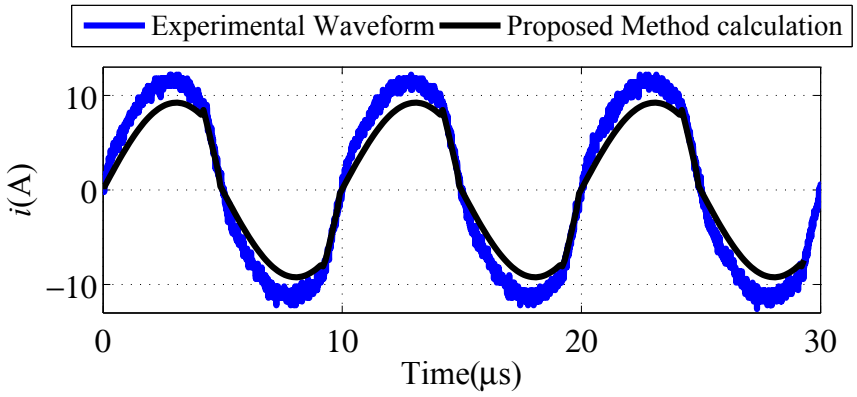

FIGURE 3.17: Experimental Current waveform compared to the current waveform obtained based on proposed method.

can be seen that the proposed method accurately predicts the simulations and experimental waveforms while providing closed form parametric equations for all the converter voltage and current signals. The small difference that is seen in the waveforms is due to the parasitics of the experimental setup like L_m of transformer, junction capacitance of the rectifier, and parasitic resistance of the resonant elements that are not included in the model of Fig. 3.1.If more accurate results are required such

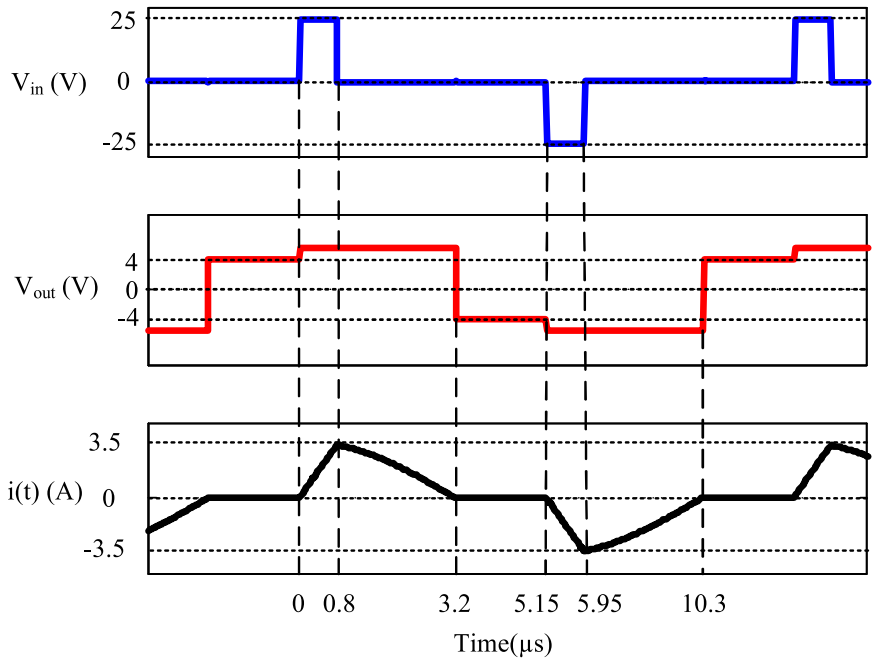

FIGURE 3.18: Simulation results for DCM operation. $d = 8\%$, $Q = 0.5 \& F = 1.23$

parasitic components should be considered in the analysis.

In order to validate the derived equations for DCM operation, converter is tested in lower output power. According to (3.29) if $F = 1.23$, for $Q \leq 0.78$ converter operates in DCM, therefore Q is selected as 0.5, or $R_L = 2.9k\Omega$ in this test. For $F = 1.23$ and $Q = 0.5$, critical duty ratio is $d_{ZVS} = 0.42$ and for duty ratios less than 0.42 converter enters DCM. In order to better show the DCM current, we choose $d = 0.08$.

According to (3.32) and (3.33) current interruption instant ($\frac{\phi}{\omega_s}$) and capacitor voltage at the interruption instant (V_{dcm}) are calculated as $3.2\mu s$ and $4V$ respectively. Figure 3.18 shows the simulation results for the above scenario, where it can be seen that the current interruption time is $3.2\mu s$ and V_{dcm} equals $4V$, which are consistent with calculated results from the proposed method.

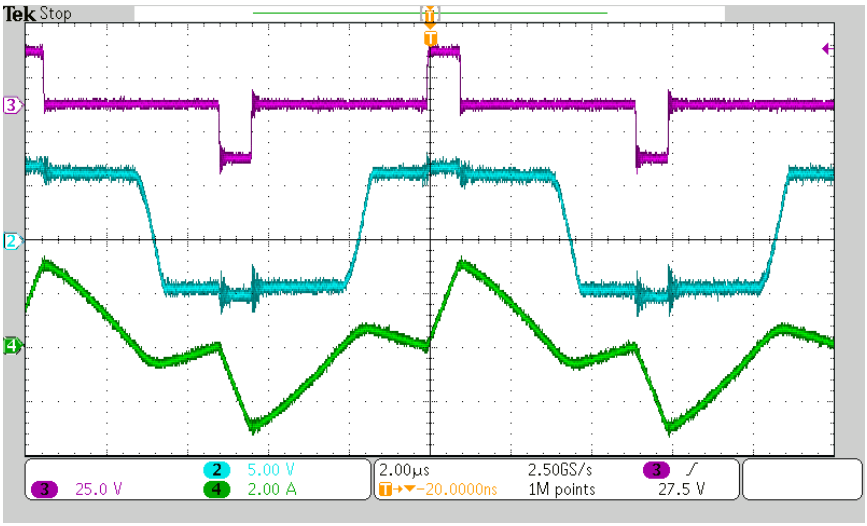

FIGURE 3.19: Experimental results for DCM operation ($V_{in} = 25$, $d = 8\%$) Ch2: Transformer primary voltage (V_{out}) with 5V/div. Ch3: Inverter voltage (V_{in}) with 25V/div. Ch4: Series current (i) with 2A/div.

Figure 3.19 shows the experimental waveforms for this test. As it can be observed in this figure, at the zero crossing, current matches with the proposed method calculations. However, current continues to conduct through junction capacitors of the output diodes, since these capacitors have relatively large value in the experimental setup. Therefore, the current does not remain exactly zero after zero crossing point and the transformer primary voltage does not remain equal to the resonant capacitor voltage. In fact, because of large junction capacitors of the rectifier diodes, converter operation is similar to the *LCC* resonant converter in DCM mode, as also reported in [34].

Using the proposed method one can use a different equivalent circuit to further investigate the junction capacitor effects on the analysis or analyze the *LCC* converter in CCM mode.

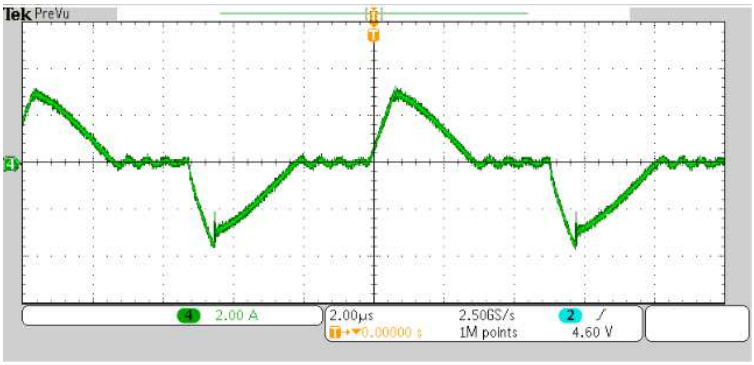

FIGURE 3.20: Experimental current waveform for DCM operation with modified gating scheme ($V_{in} = 25$, $d = 8\%$) Ch4: Series current (i) with 2A/div.

It is worth mentioning that the inverter leading leg switches turn on and off with ZCS and lagging leg switches turn on with ZVS.

In order to cease the current conduction after zero crossing point of current and to minimize the effect of the diodes junction capacitance, the gating signals of the inverter are changed in a way that the undesired current of the diodes' junction capacitance can not find a path to flow thorough the inverter. This switching scheme was first presented in [32].

Figure 3.20 shows the current waveform in this test where the current remains zero after zero crossing point. Using this gating scheme it is possible to reduce the losses of the undesired leaking current while keeping soft switching of the inverter MOSFETs.

3.5 Summary

The analysis of a full bridge Series Resonant Converter with variable duty ratio has been presented in this chapter. As the rectification stage is uncontrolled, then the

converter differential equation is non-linear, and two intermediate variables are defined to remove the non-linearity. Then using the superposition theorem converter is analyzed at steady state and intermediate variables are found in terms of main variables. It is shown that depending on duty cycle, tank parameters, and loading converter may have one of the following modes:

1. ZVS operation at CCM.
2. Hard switching operation at CCM.
3. DCM operation with ZCS.

The parametric boundary conditions between each of the above modes are obtained and analyzed along with physical interpretations. The proposed analysis is compared with the existing FCA and FS methods, and it shown that the results of proposed method is more complaint with simulations and experiments. Also it is shown that existing methods have relatively large error in calculation of converter gain, ZVS range and waveforms for far from resonant frequency operation.

Chapter 4

Series Resonant Converter Design

SRC has a vairety of applications in the literature and has been extensively adopted for renewable energy integration, voltage regulators, battery chargers, induction heating, etc[35–39].

Despite the extensive applications of SRC, very few design procedures could be found in the literature because of its complex analysis. Also the existing design procedures have many restrictions including:

1. Approximate analysis has been used and the designed SRC characteristics have significant error compared with desired characteristics[35, 37, 39].

2. Accurate modelings of the SRC have led to numerically solved equations which do not provide sufficient insight at the design stage. Therefore, trial and error methods have been used to design the SRC that results in suboptimal operation of the converter[36, 38].

3. Design of almost every parameter for the SRC is a compromise at least between two feathers of the converter. These compromises either are not discussed or have not been addressed clearly in the previous studies. For example, there is not any clear approach for snubber capacitor or transformer turns ratio selection in the proposed design procedures[26].

The accurate solutions obtained by the LBT in section 3 for SRC are used in this section to achieve an optimum converter design. Depending on the application, requirements on the converter characteristics such as voltage gain, input range, power range, etc. will be different. One of the applications of the DC/DC SRC is PV systems and DC voltage regulators, where soft switching operation is needed to achieve a high power density and high efficiency power converter. In many of these applications both the input voltage and input power vary, but the output voltage is fixed. In the literature, there are two common methods to control the output voltage of the SRC in the presence of input voltage and power variations:

1. Switching frequency control while keeping the duty cycle at the largest possible value, which is known as Pulse Frequency Modulation (PFM).

2. Fixed frequency control where duty ratio is used to regulate the output voltage. This method is also known as variable duty ratio control.

Design of power converters are normally proposed considering the control system. In other words, depending on the adopted control method, design constraints will be different. For instance, in PFM controlled SRC, the main design constraint is narrow frequency range while in fixed frequency SRC, the design constraint is the extension of the ZVS range. Therefore, design procedures for the aforementioned control schemes

will be investigated and discussed separately in the following sections. Moreover, a new control scheme is proposed to improve the performance of the converter where both duty ratio and frequency modulation are used at the same time with optimized design criteria.

4.1 Pulse Frequency Modulated SRC Design

PFM method is widely adopted in the literature, and a few design procedures are proposed for PFM controlled SRCs. Most of the existing procedures are based on iterative and approximations approaches. In this chapter, a novel design procedure based on LBT is proposed, which provides sufficient insight for the designers, without resorting to too many design iterations.

Consider the following SRC design example problem, that is common in PV systems. The requirement is to fix the output voltage at $400V$, while the input voltage may change from $V_i^{Min} = 20V$ and the power to $V_i^{Max} = 35V$, and the power can vary from $P_{Min} = 110W$ to $P_{Max} = 300W$. Resonant tank elements (L and C), snubber capacitor of the inverter switches (C_s) and transformer turns ratio (n_t) should be designed so that for the whole range of power and voltage ZVS is achieved. In the following subsections, the trade-offs of the design are discussed and a straight-forward design flowchart and criteria are presented.

4.1.1 Resonant Tank

In order to study the effects of resonant tank elements on the converter operation, a constant n_t ($n_t = \frac{N_p}{N_s} = \frac{1}{24}$) is assumed for now, and then transformer turns ratio selection criteria will be discussed later on. The resonant tank elements (L and C) could be described using ω_r and Z_0:

$$\begin{aligned} \omega_r &= \tfrac{1}{\sqrt{LC}}. \\ Z_0 &= \sqrt{\tfrac{L}{C}}. \end{aligned} \tag{4.1}$$

If the resonant frequency ω_r, and primary side reflected load resistance $n_t^2 R_L$ are considered as base frequency and impedance then the normalized switching frequency F and load quality factor Q are derived as:

$$\begin{aligned} F &= \tfrac{\omega_s}{\omega_r}. \\ Q &= \tfrac{Z_0}{n_t^2 R_L}. \end{aligned} \tag{4.2}$$

Usually switching frequency of the converter is known and thus having the F value corresponding ω_r could be obtained from (4.2). Also as n_t is given and R_L is known for any loading condition then for any operating point if Q value is given, corresponding Z_0 value is obtained. Now having ω_r and Z_0 corresponding L and C value is obtained from (4.1). Therefore, if F and Q are known for an operating point, then corresponding L and C values could be obtained. It is also observed that the value of Q is inversely related to R_L. As the output voltage is constant then R_L is inversely related to power. Therefore, Q value is directly related to power. Then, power range boundaries P_{Min}, and P_{Max} could be transformed to Q_{Min}, and Q_{Max}. Also F value is directly related to switching frequency and maximum and minimum

switching frequencies are transformed to F_{Max} and F_{Min} respectively.

Assuming a value for n_t, converter minimum and maximum gain could be obtained as follows:

$$M_{Max} = \frac{n_t V_{dcout}}{V_i^{Min}}. \tag{4.3}$$

$$M_{Min} = \frac{n_t V_{dcout}}{V_i^{Max}}. \tag{4.4}$$

To obtain F and Q values that can provide the above mentioned voltage gains, a relationship among F, Q, and M must be found. Since PFM is used, SRC always operates with maximum duty cycle, and $d = 50\%$ is substituted in:

$$\begin{aligned} M &= \left(\frac{2F}{\pi Q}\right) \frac{\sin\left(\frac{\pi d}{F}\right)}{\sqrt{\left(\frac{2F}{\pi Q}\sin\left(\frac{\pi}{2F}\right)\right)^2 + \cos^2\left(\frac{\pi}{2F}\right)}} \\ A &= \sin\left(\frac{\pi d}{F}\right)\tan\left(\frac{\pi}{2F}\right) + \cos\left(\frac{\pi d}{F}\right), \quad B = \frac{\pi Q \cos\left(\frac{\pi d'}{F}\right)}{2F\sin\left(\frac{\pi}{2F}\right)} \end{aligned} \tag{4.5}$$

After some mathematical manipulation the following relationship is obtained:

$$Q = \frac{2F}{\pi M}\left[-1 + \sqrt{1 + (1 - M^2)\tan^2(\frac{\pi}{2F})}\ \right]. \tag{4.6}$$

Equation (4.6) indicates that for any given voltage gain, there is a unique set of F and Q values that could provide this gain. This equation could be sketched in $F - Q$ plane for any desired voltage gain. Figure 4.1 shows the plot of (4.6) for M_{Max}, and M_{Min}. It can be seen that the curves are getting far from the origin by decreasing the gain from M_{Max}, to M_{Min}. In other words, for a specific power level or equivalently a specific Q value, the smaller voltage gain needs a larger F value or equivalently a larger switching frequency. Physical interpretation for this observation is that, when the converter is designed to operate at V_i^{Min} (or M_{Max}) at F_1, the drop on the tank

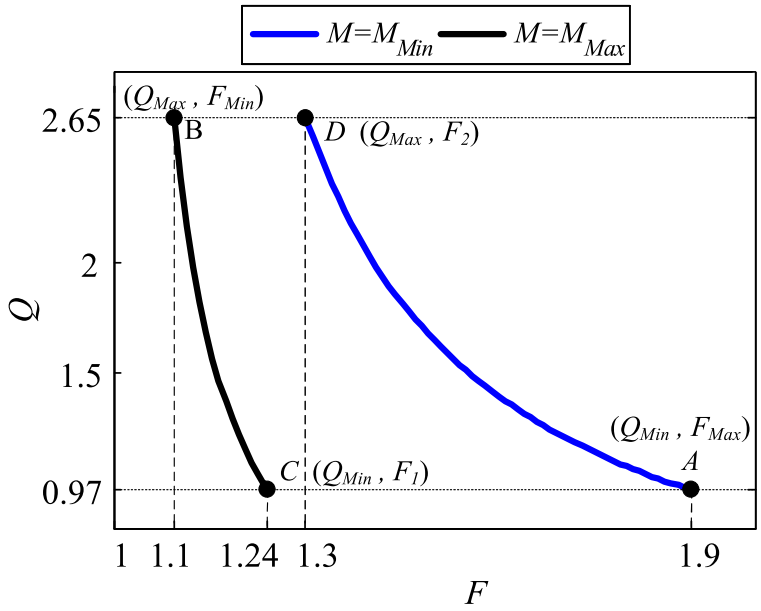

FIGURE 4.1: SRC operating area and critical operating points for minimum and maximum voltage gain.($n_t = \frac{1}{24}$, $F_{Max} = 1.9$)

should be minimum to achieve M_{Max}. For V_i^{Max} (or M_{Min}), however, F should be increased ($F > F_1$) to increase the voltage drop on the tank and reduce the gain to M_{Min}. Also, it can be seen from Fig. 4.1 that for every voltage gain, smaller power levels, or smaller Q values need larger switching frequencies. From the physical point of view, for the constant gain, constant voltage drop on resonant tank is required. However, as the power level reduces the amount of resonant current reduces and the tank impedance must be increased to compensate for the voltage drop. Thus, for any voltage gain the frequency is increased as the power decreases. In conclusion, the largest required switching frequency and consequently largest F value (F_{Max}) occurs at smallest gain (M_{Min}) and smallest power (Q_{Min}).

As the maximum allowable switching frequency of a MOSFET is limited and it is assumed to be given (ω_s is known), then the tank resonant frequency could be designed to regulate F_{Max}. If F_{Max} becomes too large, then the resonant frequency becomes too

small leading to large L and C. Increasing the F_{Max}, also will increase the frequency range, which in turn increases the physical size of magnetic components, because, they have to be designed for the smallest switching frequency. Therefore, largest F_{Max} value that does not violate the converter high power density design constraint is selected. For the design scenario presented here, F_{Max} is selected to be (1.9). As F_{Max} occurs at point A (M_{Min}, Q_{Min}), the obtained F_{Max}, along with M_{Min} derived from (4.4) are substituted in (4.6) to find Q_{Min}:

$$Q_{Min} = \frac{2F_{Max}}{\pi M_{Min}} \left[-1 + \sqrt{1 + (1 - M_{Min}^2) \tan^2(\frac{\pi}{2F_{Max}})} \right]. \tag{4.7}$$

Now that the F and Q values are known for one operating point, the corresponding L, and C could be obtained by substituting Q_{Min} and F_{Max} at (4.2).

The capacitor maximum voltage stress should also be obtained to assess the availability of such capacitor. The peak capacitor voltage occurs at current zero crossing instant ($\omega_s t = \theta$), because the derivative of the capacitor voltage is zero when the current is zero. Therefore, the peak capacitor voltage for a given operation point ($\hat{V_c}$), can be derived by writing the charge balance for the capacitor from $\omega_s t = \theta$ to $\omega_s t = \theta + \pi$:

$$Q_c = \int_{\frac{\theta}{\omega_s}}^{\frac{\theta+\pi}{\omega_s}} i(t)dt = \frac{\pi}{R_L \omega_s} n_t V_{dcout}. \tag{4.8}$$

In this period, capacitor voltage is changed from $-\hat{V_c}$ to $+\hat{V_c}$:

$$Q_c = C \times 2\hat{V_c}. \tag{4.9}$$

Thus $\hat{V_c}$ is obtained as:

$$\hat{V_c} = \frac{\pi}{2R_L C \omega_s} n_t V_{dcout}. \tag{4.10}$$

Using (4.2), $\hat{V_c}$ is obtained in terms of F and Q as:

$$\hat{V_c} = \frac{\pi Q}{2F} n_t V_{dcout}. \tag{4.11}$$

According to (4.11) the maximum of $\hat{V_c}$ for all operating conditions occurs at point B (Q_{Max},F_{Min}), where $F_{Min} \approx 1$. According to Q definition:

$$Q = \frac{Z_0}{n_t^2 R_L} = \frac{Z_0}{n_t^2 V_{dcout}^2} P. \tag{4.12}$$

Therefore $Q_{Max}/Q_{Min} = P_{Max}/P_{Min}$. Thus, capacitor maximum voltage stress is obtained as:

$$V_c^{stress} = Max\{\hat{V_c}\} = \frac{\pi P_{Max} Q_{Min}}{2P_{Min}} n_t V_{dcout}. \tag{4.13}$$

Substituting Q_{Min} from (4.7) in (4.13) results in:

$$V_c^{stress} = \frac{P_{Max}}{P_{Min}} n_t V_{dcout} \frac{F_{Max}}{M_{Min}} \left[-1 + \sqrt{1 + (1 - M_{Min}^2) \tan^2(\frac{\pi}{2F_{Max}})} \right]. \tag{4.14}$$

Having the F_{Max} determined from power density constraint as well as M_{Min} from n_t, the capacitor stress could be determined from (4.14). If a capacitor with such voltage stress is provided by vendors then the design is feasible. However, if the voltage stress is higher than the voltage limit specified by the vendor (V_c^{limit}), then another F_{Max} value should be chosen. Figure 4.2 is the plot of (4.14) for the above mentioned design scenario with $n_t = \frac{1}{24}$. It is observed that as larger F_{Max} is selected, the capacitor voltage stress decreases. However, further increasing F_{Max} will lead to lower power density design. Therefore, F_{Max} should be increased just to the amount that the corresponding voltage stress is equal to capacitor voltage limit (V_c^{limit}).

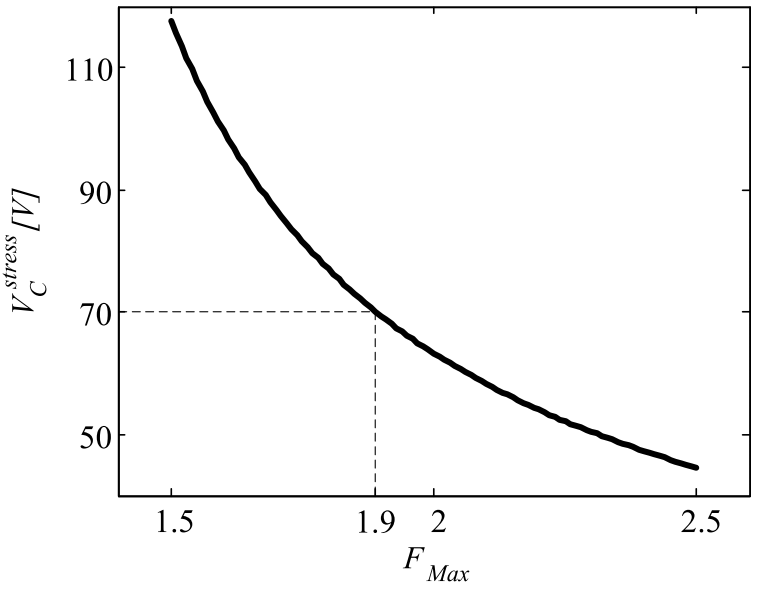

FIGURE 4.2: Resonant capacitor voltage stress versus selected F_{Max} value for the design.

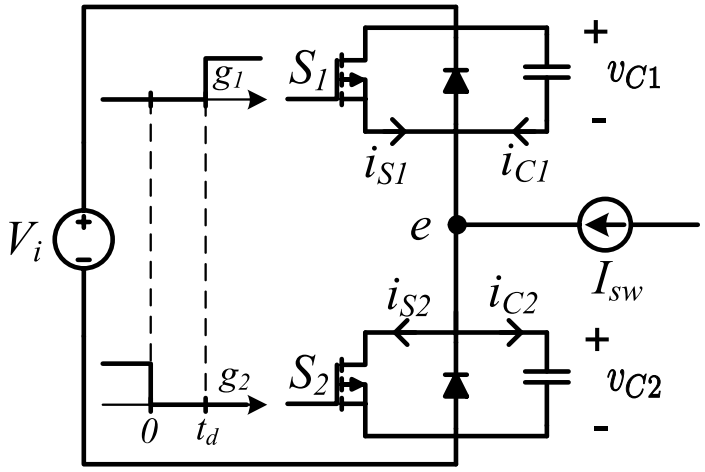

FIGURE 4.3: Leading leg switches with corresponding snubber capacitor at the switching instant ($\omega_s t = 0$)

It is worth noting that the relation between F and Q values providing the gain M is obtained from LBT method. As shown in chapter 3 if other existing methods were used, the calculated gain would become inaccurate and could result in converter failure to cover the required input voltage range. Conventionally a large margin was

used for gain selection to avoid the converter's failure to cover the input voltage range.

Also the capacitor voltage stress relation with the frequency range of the converter was never expressed using the closed form formula. In this study the closed form equation obtained for voltage stress from LBT method could be used to select the appropriate amount of frequency range. In the previous methods, first frequency range was selected then the capacitor voltage stress was found and this iteration was repeated until the capacitor stress was tolerable.

4.1.2 Snubber Capacitor Design

To find the optimum snubber capacitor, first the switching losses must to be studied. As the resonant current and input square wave voltage are half-wave symmetrical, then the switching losses for all switches will be the same. Thus, the turn on and turn off switching losses could be obtained by studying the switching instant for only one leg. When SRC is working with $d = 50\%$, the switchings occur at $\omega_s t = 0$ and $\omega_s t = \pi$. Thus, the switching of the leading leg (S_1 and S_2) is only studied at $\omega_s t = 0$. As it is shown in Fig. 4.3 at $\omega_s t = 0$ the gate signal of switch S_2 is removed and the dead-time between two switches starts. After the dead-time (t_d), which is usually 1 or 2 percent of the switching period, the gate signal for the switch S_1 is applied. As the dead-time is much smaller than the switching period, then the resonant current does not change considerably during the dead-time and can be assumed as a constant current equal to the resonant current at $\omega_s t = 0$. To achieve ZVS, the current at $\omega_s t = 0$ should be negative, which is denoted by $-I_{sw}$. The switching losses are

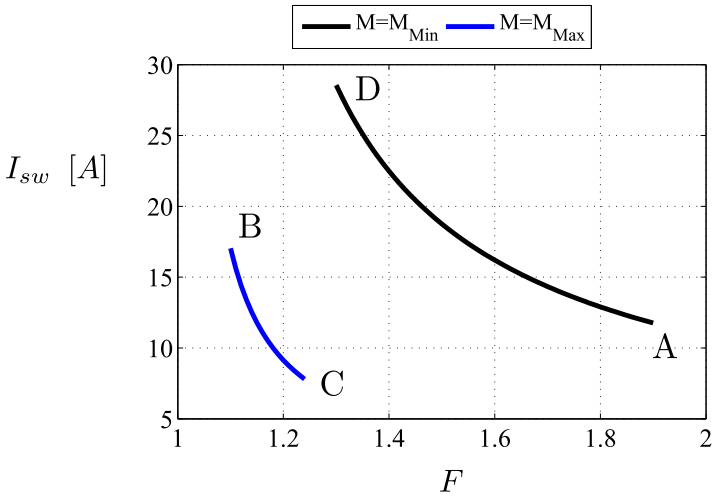

FIGURE 4.4: switching current I_{sw} versus F for constant M.

dependent on I_{sw}, which can be derived using LBT from (3.21) as below:

$$I_{sw} = V_i C \omega_r \left(1 - M^2\right) \tan(\frac{\pi}{2F}). \tag{4.15}$$

Figure 4.4 shows I_{sw} versus F for constant gains of M_{Min} and M_{Max}. It can be observed that the maximum and minimum switching currents occur at points D and C respectively.

As shown in Fig. 4.5 before $t = 0$, I_{sw} flows through S_2. When the gate signal of S_2 is zero, i_{S2} falls linearly and it reaches zero during the MOSFET fall time ($t = t_f$). The current deviated from S_2 has no path to flow except through the snubber capacitors of the switches:

$$v_{C1} + v_{C2} = V_{dc} \implies C_1 \frac{dv_{C1}}{dt} + C_2 \frac{dv_{C2}}{dt} = 0 \tag{4.16}$$

$$\implies i_{C1} = -i_{C2}. \tag{4.17}$$

KCL at node e results in:

$$I_{sw} = 2i_{C2} + i_{S2}. \tag{4.18}$$

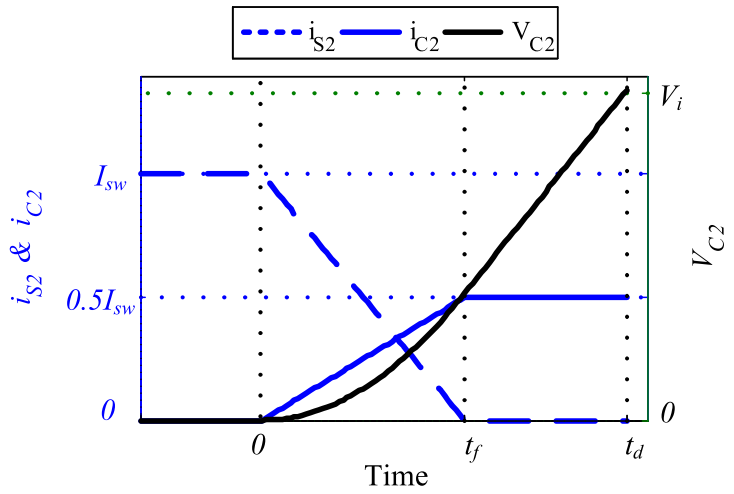

FIGURE 4.5: switching voltage and current waveform for the switch S_2.(t_f current fall time, t_d dead-time)

As during the dead-time $i_{S2} = 0$, i_{C2} rises linearly form zero at $t = 0$ to $0.5I_{sw}$ at $t = t_f$. From t_f to the end of dead-time, i_{C2} remains at $0.5I_{sw}$. The voltage across S_2 is equal to v_{C2}:

$$v_{C2}(t) = \frac{1}{C_2}\int_0^t i_{C2}(\tau)d\tau = \begin{cases} \int_0^t \frac{I_{sw}}{2C_s}\frac{\tau}{t_f}d\tau = \frac{I_{sw}}{4C_s t_f}t^2 & 0 \le t \le t_f \\ \frac{I_{sw}}{4C_s}t_f + \int_{t_f}^t \frac{I_{sw}}{2C_s}d\tau = \frac{I_{sw}}{4C_s}t_f + \frac{I_{sw}}{2C_s}(t - t_f) & t_f \le t \le t_d \end{cases} \tag{4.19}$$

The voltage across S_2 is zero at $t = 0$, and it is a parabolic function of time until t_f, and is linear after t_f. It can be observed that the switches turn on with zero voltage and the snubber capacitor is discharged before the switch turns on and its energy is restored. Therefore, the amount of snubber capacitor could be increased to decrease the slope of voltage rise at turn off instant and consequently decrease the turn off loss. Now using the voltage and current waveforms, turn off switching loss is calculated as:

$$P_{off} = \frac{I_{sw}^2}{C_s}\frac{t_f^2 f_s}{48}. \tag{4.20}$$

At the turn on instant, it should be mentioned that obtaining full ZVS is the only way to eliminate the turn on losses. To achieve the full ZVS at turn on, C_1 should be discharged completely and v_{C1} should reach zero before the end of dead-time. As $v_{C1} + v_{C2} = V_i$, in order for v_{C1} to reach zero, v_{C2} has to reach V_i at the end of dead-time. Using (4.19), v_{C2} at the end of dead-time is:

$$v_{C2}(t_d) = \frac{I_{sw}}{C_s}\left(\frac{t_d}{2} - \frac{t_f}{4}\right). \tag{4.21}$$

If $v_{C2}(t_d) = V_i$ then the maximum snubber capacitance that could be completely discharged is derived as:

$$C_s = \frac{I_{sw}}{V_i}\left(\frac{t_d}{2} - \frac{t_f}{4}\right). \tag{4.22}$$

There is a trade-off for C_s selection. Increasing C_s, reduces the turn off switching losses but at the same time, requires a higher I_{sw} to get full ZVS. Therefore, the snubber capacitor is selected as the largest capacitor that does not violate ZVS even under worst case scenario. According to (4.22) worst case scenario for ZVS occurs when $\frac{I_{sw}}{V_i}$ is the smallest possible value. According to (4.15):

$$\frac{I_{sw}}{V_i} = C\omega_r\left(1 - M^2\right)\tan(\frac{\pi}{2F}). \tag{4.23}$$

Therefore, for every voltage gain, smallest $\frac{I_{sw}}{V_i}$ is obtained at largest F. According to (4.15) and (4.22) worst case scenario for ZVS occurs at point C (Q_{Min},F_1) (see Fig. 4.1) for the discussed design problem. Therefore optimum sunbber capacitor is derived as:

$$C_s^{opt} = C\omega_r\left(1 - M_{Max}^2\right)\tan(\frac{\pi}{2F_1})\left(\frac{t_d}{2} - \frac{t_f}{4}\right). \tag{4.24}$$

According to (4.20) it can be observed that the worst case scenario for turn off switching loss occurs for the largest I_{sw}. For the design problem described here worst case for turn off loss occurs at point D. Then the normalized turn off loss at worst case is obtained as:

$$\frac{P_{off}}{P_{Min}} = \frac{1}{Q_{Min}} \frac{\left(1 - M_{Min}^2\right)^2}{M_{Min}^2 \left(1 - M_{Max}^2\right)} \frac{\tan^2(\frac{\pi}{2F_2})}{\tan(\frac{\pi}{2F_1})} \frac{t_f^2 f_s}{12\left(2t_d - t_f\right)}. \tag{4.25}$$

Where, P_{Min} is the minimum power that is specified in design requirements, and as shown in Fig. 4.1 F_1 and F_2 are the normalized switching frequencies at which SRC is able to provide M_{Max} at Q_{Min} and M_{Min} at Q_{Max} respectively.

The selection of snubber capacitance is directly dependent on switching current calculation. As shown in chapter 3 other existing methods ignore the current waveform large signal distortions and thus the obtained switching current could be highly inaccurate and leads to inappropriate selection of C_s and consequently damage to switches.

Also using the obtained formulas from LBT method it is shown that worst case scenario for the turn on and turn off switching loss occurs at point C and D which makes the design of snubber capacitor more straightforward.

4.1.3 Transformer Turns Ratio

n_t is the ratio of transformer primary turns to secondary turns and therefore:

$$n_t = \frac{N_p}{N_s} = \frac{V_o}{V_{dcout}}. \tag{4.26}$$

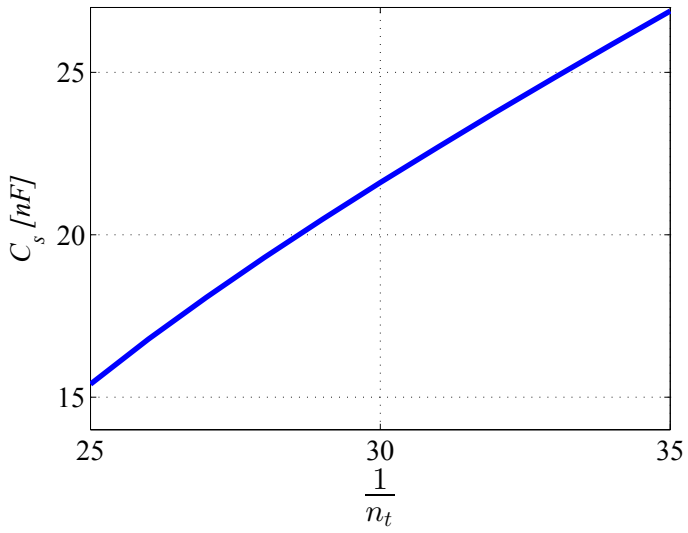

FIGURE 4.6: Snubber capacitance (C_s) for different selection of n_t.

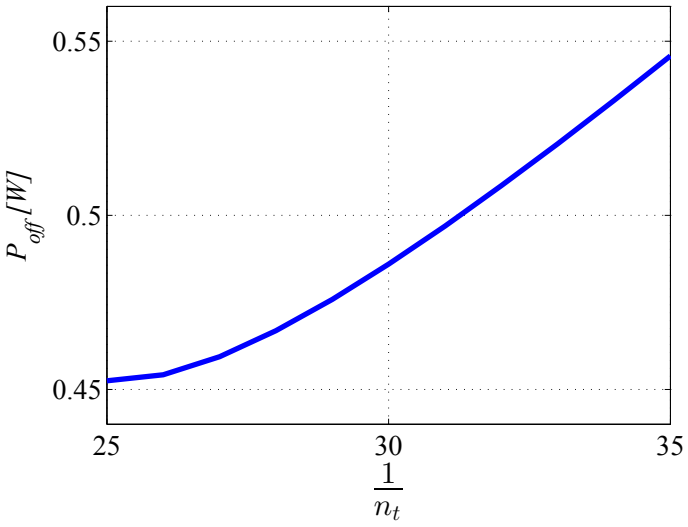

FIGURE 4.7: Turn off switching loss (P_{off}) for different selection of n_t.

Also voltage gain of the resonant tank is:

$$M = \frac{V_o}{V_i}. \tag{4.27}$$

Therefore, the total gain of the converter could be written as:

$$\text{Total Gain} = \frac{V_{dcout}}{V_i} = \frac{M}{n_t}. \tag{4.28}$$

Therefore, when $V_i = V_i^{Min}$, maximum total gain is needed. When V_i increases up to V_i^{Max}, M can be adjusted by F to reduce the total gain. Thus n_t should guarantee the required maximum total gain at M_{Max}. Therefore, the highest n_t that may be needed (n_t^{start}) is:

$$\frac{V_{dcout}}{V_i^{Min}} = \frac{M_{Max}}{n_t^{start}} = \frac{1}{n_t^{start}}. \tag{4.29}$$

depending on C_s lower n_t may be needed.

Decreasing n_t from n_t^{start}, results in increase of both primary side current and conduction losses. However, higher current provides a better turn on ZVS and as indicated by (4.22), allows the use of larger snubber capacitance but ultimately leads to increased turn off switching losses. Thus, transformer turns ratio selection is a compromise between the minimum required capacitor for turn on ZVS and conduction and turn off losses.

Figure 4.6 and 4.7 show plot of C_s and P_{off} for different values of n_t according to (4.24) and (4.25). In general, optimum n_t is n_t^{start} that provides lowest conduction and switching losses. However, depending on the design specifications, n_t^{start} could result in a C_s^{opt} value that is smaller than MOSFET inherent junction capacitor C_{ds}. In that case, I_{sw} can not even discharge C_{ds} and ZVS will be lost. Thus, n_t must be reduced so that ZVS operation is guaranteed.

Using the LBT method a clear approach for n_t selection is proposed here that is based on closed form equations and does not lead to too many iterations. In the previous

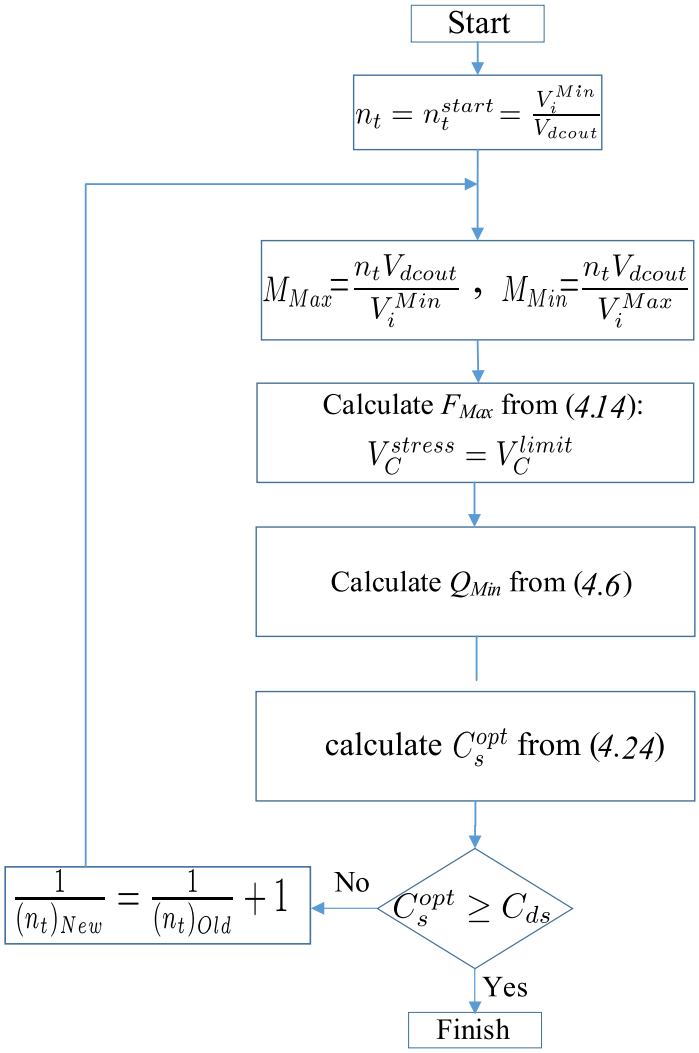

FIGURE 4.8: Design flowchart.

design procedures n_t selection was based on the designer's own experience in that application rather than a general selection criteria.

Flowchart in Fig. 4.8 summarizes the proposed design procedure. In the design problem of this section, the obtained parameters are shown in table 4.1.

Parameter	Value
Resonant inductance L	$5.1\mu H$
Resonant capacitance C	$0.8\mu F$
Transformer ratio $\frac{N_p}{N_s}$	$\frac{1}{24}$
Snubber capacitance C_s^{opt}	$1.5nF$

TABLE 4.1: Obtained parameters for PFM controlled SRC.

4.2 Fixed Frequency SRC Design

The Pulse Frequency Modulation control cannot be used in all applications due to the following restrictions:

1. The size of components are designed for smallest frequency that results in larger physical size of magnetic components. Therefore, PFM controlled SRC offers less power density, compared with variable duty cycle controlled SRC.

2. Due to frequency variations, EMI emissions of the the PFM controlled SRC cannot be suppressed easily, and it cannot be used in EMI sensitive applications.

The fixed frequency SRC has been widely used in the literature for many applications including voltage regulator modules for Microprocessors and Application Specific ICs. Power density is a crucial factor for these applications and also EMI emissions cannot be tolerated. Therefore, PFM method cannot used for these applications and Variable Duty cycle control at the fixed frequency is normally used to regulate the voltage. Since the duty ratio may decrease for specific loads and input voltages, it is possible to reach duty ratios less than ZVS duty ratio d_{ZVS}, which causes hard-switching operation and damage to the converter.

The boundary for ZVS operation is specified by d_{ZVS} in chapter 3 at (3.28), which was for ideal conditions. In practice, the non-idealities will affect d_{ZVS}. Among all non-idealities the effect of dead time between inverter switches is the most important factor, especially for high frequency resonant converters where the dead-time is a significant portion of the switching period. Therefore, in the following subsection, the effect of dead time on the SRC characteristics is discussed to provide a better insight for fixed frequency SRC design.

4.2.1 Dead-time effects

The process that occurs during the dead-time for the ZVS operation of SRC is illustrated in section 4.1.2. If SRC operates with ZVS, then during the dead-time, drain-source capacitance (C_{ds}) of the switch pairs in a leg are charged and discharged by the current that is drawn by resonant tank. In fact, the amount of resonant current at the switching instant determines the charging and discharging rate of the switches. For the hard switching operation of the inverter the process of the switching transition is completely described in [40] for which a Miller plateau is normally observed. As soft switching operation of the SRC is normally a design requirement, in this section, the dead-time effects are only studied for soft switching (ZVS) cases.

As shown in Fig. 4.5, during the dead-time, the voltage across the (C_{ds}) which is the inverter terminal voltage ($v_{in}(t)$), has two segments. Firstly, it raises as a parabolic function of time, then it rises linearly until it reaches to the V_i value. The rate of voltage increase is determined by the amount of resonant current at switching instant (I_{sw}). For the sake of simplicity it is assumed that the voltage increases linearly during the dead-time.

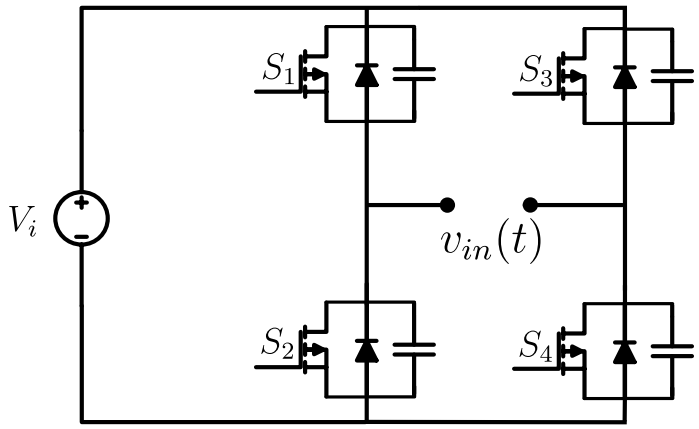

FIGURE 4.9: Inverter topology for full bridge SRC.

Figure 4.9 shows the inverter topology for the full bridge SRC. Switches S_3 and S_4 that form the lagging leg, regardless of duty cycle always turn off with negative current and thus operate with Zero Voltage Switching (ZVS). Therefore, a large snubber capacitance could be selected for the lagging leg switches to reduce the turn off losses as well. However, switches S_1 and S_2 that form the leading leg are vulnerable to loss of ZVS under low duty cycles and need a precise selection of the snubber capacitance and dead-time.

Assuming that the voltage increases linearly during the dead-time, the effect of dead-time on the inverter voltage is shown in Fig. 4.10. All the switches are working at 50 percent duty cycle, however the phase shift between two legs determines the duty cycle of generated $v_{in}(t)$.

For the non-ideal case, the gate signal of the switch that has to conduct next, is applied with some delay which is called dead-time. During the dead-time $v_{in}(t)$ increases/decreases linearly until it reaches to $+V_i$ or $-V_i$. Usually the amount of

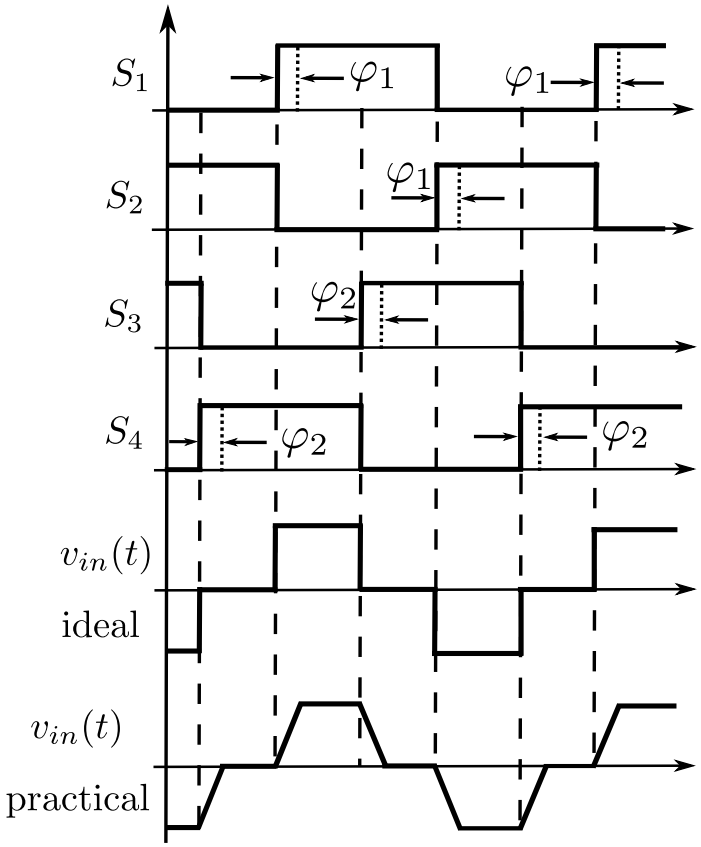

FIGURE 4.10: Effects of dead-time on the inverter terminal voltage $v_{in}(t)$.

dead-time is regulated in a way that the voltage increase/decrease finishes at the end of dead-time. The time that is needed for voltage increase/decrease is directly dependent on the amount of current at switching instant I_{sw} and C_s. Switches S_1 and S_2 turn off at equal I_{sw}, and switches S_3 and S_4, both turn off at equal but larger value of I_{sw}. Therefore, the dead-time of S_1 and S_2 is the same and is denoted by φ_1, while the dead-time of S_3 and S_4 is denoted by φ_2. In general $\varphi_1 \leq \varphi_2$, however, for $d = 50\%$ (square wave operation) $\varphi_1 = \varphi_2$ and they have the largest possible value. As it will be shown later, the most important effect of the dead-time non-ideality is its influence on the ZVS range for which the maximum dead-time is the worst case scenario. Therefore, in the non-ideal waveform of the $v_{in}(t)$ which is shown in

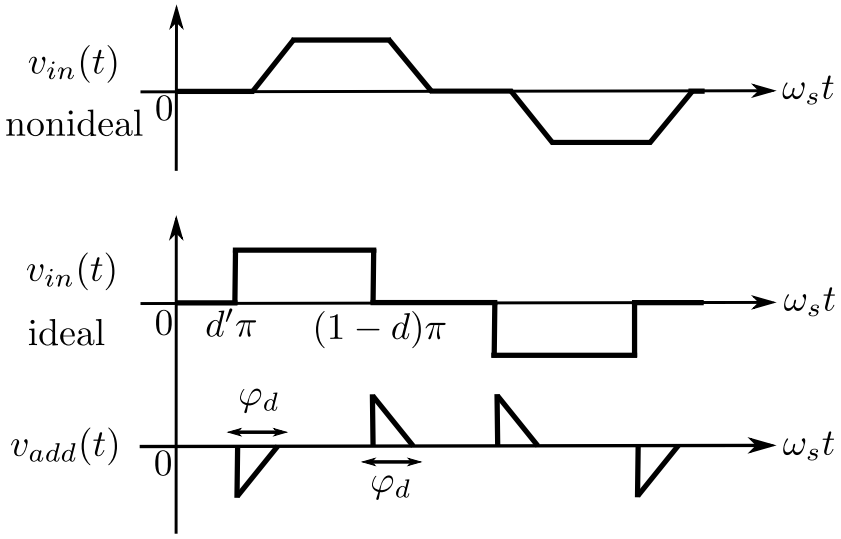

FIGURE 4.11: Decomposition of the non-ideal waveform of the $v_{in}(t)$.

Fig. 4.10 it is assumed that $\varphi_1 = \varphi_2 = \varphi_d$. It is important to note that the non-ideal waveform is shifted to the right by $\frac{\varphi_d}{2}$.

In order to apply the LBT for analysis of SRC with the dead-time effect, as shown in Fig. 4.11, the non-ideal waveform is decomposed into two waveforms, ideal waveform and a ramp function. The superposition law is used to analyze the SRC. Applying the LBT to the ideal waveform is described in section 3.1 that results in following initial conditions:

$$\begin{aligned} V_{0,id} &= 0 \\ V'_{0,id} &= -V_i \omega_r \frac{\sin\left(\frac{\pi d}{F}\right)}{\cos\left(\frac{\pi}{2F}\right)}. \end{aligned} \tag{4.30}$$

The Laplace transform of the $v_{add}(t)$ could be easily obtained as:

$$\begin{aligned} V_{add}(s) = \frac{V_i}{s} &\left[e^{-s\frac{\varphi_d + d'\pi}{\omega_s}} - e^{-s\frac{d'\pi}{\omega_s}} - e^{-s\frac{\varphi_d + d'\pi = 2\pi d}{\omega_s}} - e^{-s\frac{(1-d)\pi}{\omega_s}} \right] \\ + \frac{\varphi_d V_i}{2\omega_s} &\left[e^{-s\frac{d'\pi}{\omega_s}} - e^{-s\frac{(1-d)\pi}{\omega_s}} \right]. \end{aligned} \tag{4.31}$$

Then, $V_{0,add}$ and $V'_{0,add}$ are derived by plugging $s = \pm j\omega_r$ into $G(s) = -V_{add}(s)$:

$$\begin{aligned} V_{0,add} &= -V_i \left[\frac{\varphi_d}{2F} \frac{\sin(\frac{\pi d}{F})}{\cos(\frac{\pi}{2F})} + \left(\cos(\frac{\varphi_d}{F}) - 1 \right) \right] \\ V'_{0,add} &= V_i \omega_r \sin\left(\frac{\varphi_d}{F}\right). \end{aligned} \tag{4.32}$$

These initial conditions are added to find the steady state initial conditions for the non-ideal waveform:

$$\begin{aligned} V_0 &= -V_i \left[\frac{\varphi_d}{2F} \frac{\sin(\frac{\pi d}{F})}{\cos(\frac{\pi}{2F})} + \left(\cos(\frac{\varphi_d}{F}) - 1 \right) \right] \\ V'_0 &= V_i \omega_r \sin\left(\frac{\varphi_d}{F}\right) - V_i \omega_r \frac{\sin\left(\frac{\pi d}{F}\right)}{\cos\left(\frac{\pi}{2F}\right)}. \end{aligned} \tag{4.33}$$

It is worth noting that $V_{0,add}$ and $V'_{0,add}$ become zero for $\varphi_d = 0$. However, the effect of $v_{add}(t)$ on the ODE Zero State Response has to be included to find the final exact solution.

$v_{add}(t)$ is always zero except during the dead-time where it is equal to a ramp function. Therefore, the Zero State Response of the SRC Ordinary Differential Equation to the ramp function has to be obtained in order to study the effects of $v_{add}(t)$ in time domain. The Unit Ramp Response ($URR(t)$) of the SRC's ODE is derived as:

$$LC\ddot{v_c}(t) + v_c(t) = t, \qquad v_c(0) = \dot{v_c}(0) = 0. \tag{4.34}$$

That results in following unit ramp response:

$$URR(t) = \frac{F}{\omega_s} \left(\omega_r t - \sin(\omega_r t) \right). \tag{4.35}$$

As it can be observed from (4.35), the ZSR of $v_{add}(t)$ contains both algebraic (t) and

trigonometric functions ($\sin(\omega_r t)$) of time, which makes it difficult to find the analytical solution for converter characteristics like SRC voltage gain M and its current zero crossing angle θ. Therefore, the Taylor expansion of the trigonometric functions could be used in the analysis:

$$\begin{aligned} \sin(x) &= x - \tfrac{x^3}{3!} + \tfrac{x^5}{5!} + ... \\ \cos(x) &= 1 - \tfrac{x^2}{2} + \tfrac{x^4}{4!} + ... \end{aligned} \tag{4.36}$$

Thus, if $x \to 0$, the Higher Order Terms could be neglected:

$$\begin{aligned} \sin(x) &\approx x \\ \cos(x) &\approx 1 \end{aligned} \tag{4.37}$$

Since φ_d is very small (dead-time is a very small portion of the switching period) and the unit ramp response is evaluated for the $[0 \quad \varphi_d]$ the effect of unit ramp response can be approximated zero and can be completely neglected. Therefore, the only function that determines the ZSR is the ideal waveform which has not been altered. In fact using the (4.37) we can approximate the ZSR of the non-ideal waveform by the ZSR of the ideal case. Also if (4.37) is substituted in (4.32) it can be concluded that the steady state initial conditions obtained for the non-ideal waveform is approximately equal to the state of the ideal SRC at $\omega_s t = \frac{\varphi_d}{2}$. Thus, the system's time domain response will follow the same intervals that an ideal response follows, however, compared to ideal case the response to the non-ideal waveform will starts from $\frac{\varphi_d}{2}$. In other words, to get the non-ideal response, it is sufficient to shift the ideal response to the right by $\frac{\varphi_d}{2}$. Therefore, SRC gain M will not be affected if the non-ideality of dead-time is considered, however, the current phase shift θ will become $\theta + \frac{\varphi_d}{2}$.

In order to show the validity of the approximation for the non-ideal dead-time analysis, some simulation are carried out for the SRC with non-ideal waveform. The simulation parameters are summarized in table 4.2.

Parameter	Value
Normalized frequency$F$	1.3
Quality factor Q	2
Transformer ratio $\frac{N_p}{N_s}$	1
Input voltage V_i	$100V$
duty cycle d	0.35

TABLE 4.2: Parameters used for SRC simulation with dead-time non-ideality.

Simulations have been carried out with three different φ_d values, and results are shown in table 4.3.

$\frac{\varphi_d}{2\pi}$	M	$\theta - \frac{\varphi_d}{2}$	$i(d'\pi)$	$i(d'\pi + \varphi_d)$	$i\left(d'\pi + \frac{\varphi_d}{2}\right)$
0.5%	0.51	0.88 (rad)	-3.4	-3.2	-3.27
1%	0.51	0.88 (rad)	-3.5	-3	-3.25
5%	0.51	0.88 (rad)	-4	-1.9	-3.16

TABLE 4.3: Dead-time non-ideality effects on SRC characteristics.

It can be observed that the SRC gain is independent of φ_d value. Also the amount of current at $\omega_s t = d'\pi$ is dependent on φ_d and increases as the φ_d increases. However, the amount of current at $\omega_s t = d'\pi + \frac{\varphi_d}{2}$ is almost independent of φ_d. Furthermore, if the $\frac{\varphi_d}{2}$ shift is considered then the current phase lag θ will be independent of φ_d. Another observation is that the amount of current right at the middle of switching transition (at $d'\pi + \frac{\varphi_d}{2}$) is the average value of the current in the $[d'\pi \quad d'\pi + \varphi_d]$, and thus $i\left(d'\pi + \frac{\varphi_d}{2}\right)$ could be used for snubber calculations.

4.2.2 Practical D_{ZVS} Calculation

After considering the effects of the dead-time non-ideality on the SRC analysis, the real ZVS range in the presence of dead-time could be calculated. The necessary condition for the ZVS in presence of dead-time (or $C_{ds} \neq 0$) is that the current remains negative until the end of dead-time. In fact for theoretical ZVS range the ideal current waveform at switching instant $\omega_s t = d'\pi$ has to be zero, while for practical case the non-ideal current waveform at $\omega_s t = d'\pi + \varphi_d$ has to be zero. As the non-ideal waveform is the shifted version of ideal waveform by $\frac{\varphi_d}{2}$, the ZVS condition is that the practical current zero crossing occurs at the end of dead-time:

$$d'\pi + \varphi_d = \theta + \frac{\varphi_d}{2}. \tag{4.38}$$

which results in:

$$\frac{\varphi_d}{2} = \theta - d'\pi. \tag{4.39}$$

Basically φ_d is known because the maximum dead-time that is the worst case scenario for (4.39) is known. However, the right side of the (4.39) is nonlinear, and first it has to be linearized and then solved to find the practical ZVS duty cycle D_{ZVS}. Since the practical ZVS duty ratio (D_{ZVS}) is close to the theoretical ZVS duty ratio (d_{ZVS}), right side of (4.39) is linearized around the theoretical d_{ZVS}.

$$\theta - d'\pi = f(d) \approx f(d_{ZVS}) + \left(\frac{\partial f}{\partial d}\right)_{d=d_{ZVS}} \times \Delta d = 0 + \left(\left(\frac{\partial \theta}{\partial d}\right)_{d=d_{ZVS}} + \pi\right) \times \Delta d. \tag{4.40}$$

Therefore, practical ZVS duty cycle D_{ZVS} is obtained as:

$$D_{ZVS} = d_{ZVS} + \Delta d. \tag{4.41}$$

Where Δd is:

$$\Delta d = \frac{\frac{\varphi_d}{2}}{\left(\left(\frac{\partial\theta}{\partial d}\right)_{d=d_{ZVS}} + \pi\right)}. \tag{4.42}$$

According to θ formula in (3.23), the formula used for θ calculation is different for $d > d_{d_{ZVS}}$ and $d < d_{ZVS}$. As $D_{ZVS} > d_{ZVs}$, the following formula for θ is being used:

$$\theta = \frac{\pi}{2} - F\sin^{-1}\left(M\frac{\sin\frac{\pi}{2F}}{\cos\frac{\pi d'}{F}}\right). \tag{4.43}$$

$\left(\frac{\partial\theta}{\partial d}\right)_{d=d_{ZVS}}$ is calculated as:

$$\left(\frac{\partial\theta}{\partial d}\right)_{d=d_{ZVS}} = \frac{2\cos\left(\gamma\left(1-4d_{ZVS}\right)\right) - \frac{\sin\gamma}{\gamma}\times\left(\frac{\partial M}{\partial d}\right)_{d=d_{ZVS}}}{\cos\gamma + \cos\left(\gamma\left(1-4d_{ZVS}\right)\right)}\pi - \pi. \tag{4.44}$$

Therefore, Δd is obtained as below:

$$\Delta d = \frac{\varphi_d}{2\pi}\left[\frac{\cos\gamma + \cos\left(\gamma\left(1-4d_{ZVS}\right)\right)}{2\cos\left(\gamma\left(1-4d_{ZVS}\right)\right) - \frac{\sin\gamma}{\gamma}\times\left(\frac{\partial M}{\partial d}\right)_{d=d_{ZVS}}}\right]. \tag{4.45}$$

Where $\gamma = \frac{\pi}{2F}$ and also $\left(\frac{\partial M}{\partial d}\right)_{d=d_{ZVS}}$ is derived from:

$$M = \left(\frac{2F}{\pi Q}\right)\frac{AB\sqrt{A^2+B^2-1} - B^2}{A^2+B^2}. \tag{4.46}$$

$$A = \sin\left(\frac{\pi d}{F}\right)\tan\left(\frac{\pi}{2F}\right) + \cos\left(\frac{\pi d}{F}\right), \quad B = \frac{\pi Q\cos\left(\frac{\pi d'}{F}\right)}{2F\sin\left(\frac{\pi}{2F}\right)}$$

Therefore, $\left(\frac{\partial M}{\partial d}\right)_{d=d_{ZVS}}$ is obtained as:

$$\left(\frac{\partial M}{\partial d}\right)_{d=d_{ZVS}} = \frac{2\gamma^2 Q\cot\gamma}{\sin\gamma}\left[\frac{\sin\beta}{\sqrt{1+(\gamma Q\cot\gamma)^2}} + \frac{\cos\beta}{\sin\gamma\left[1+(\gamma Q\cot\gamma)^2\right]^{\frac{3}{2}}}\right]. \tag{4.47}$$

β used in (4.47) is:

$$\beta = \arctan\left(\frac{\tan\gamma}{\gamma Q}\right) + \gamma - \frac{\pi}{2}. \tag{4.48}$$

Therefore, as for every F and Q pair, there is a unique theoretical ZVS duty cycle d_{ZVS}, there is also a practical ZVS duty cycle (D_{ZVS}) for every F and Q. Practical ZVS duty cycle d_{ZVS} also depends on φ_d that is determined based on maximum dead-time, and in this study it has been assumed that $\varphi_d = 0.01 \times 2\pi$. Figure 4.12 shows the practical and theoretical ZVS duty cycle versus Q for a constant F. It is observed that practical ZVS duty cycle is always greater than the theoretical ZVS duty cycle, however, the difference Δd is a non-linear function of F and Q. It also can be observed that for $d_{ZVS} = 0.05$ the amount of Δd is almost equal to d_{ZVS} itself and D_{ZVS} calculation may be inaccurate. Therefore, the calculation of D_{ZVS} is most accurate if d_{ZVS} is larger than 0.05.

4.2.3 Fixed Frequency Control Design Procedure

As discussed earlier, for the fixed frequency SRC, the voltage regulation is achieved by controlling the duty cycle while the switching frequency or the F value is constant. As a simple example consider that SRC is designed to convert a constant input DC voltage into a constant output DC voltage (constant M is required), however, the load could be changed. The load variations change the Q value, and Q variations in

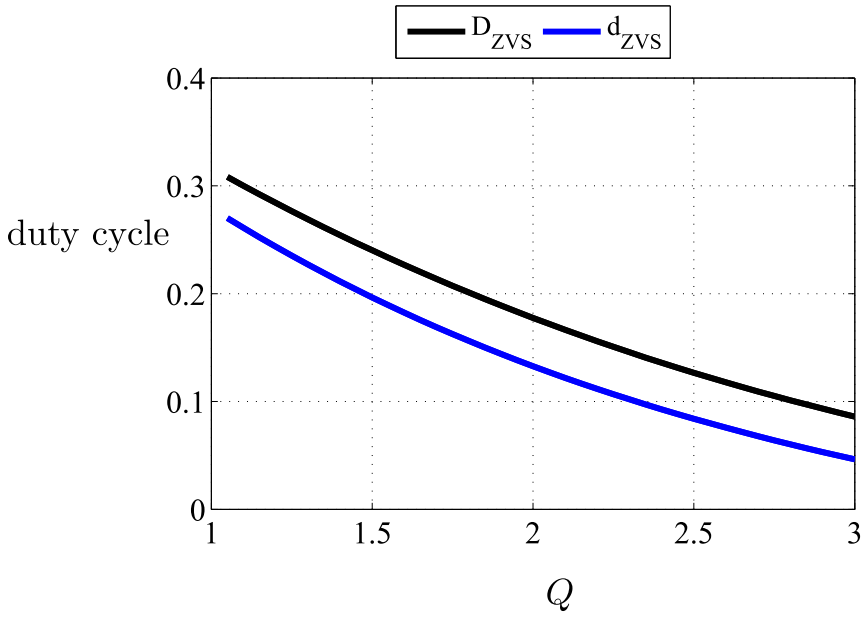

FIGURE 4.12: Practical and theoretical ZVS duty cycle versus Q for constant F ($F = 1.4$).

turn change the gain value M. Figure 4.13 is the plot of equation (3.26) and shows the gain characteristic versus duty cycle for a constant F value. It can be observed that the gain value increases as Q decreases and duty cycle has to be reduced to get a constant gain value. Therefore, SRC first has to be designed to provide the designated gain with $d = 50\%$ at Q_{Max} (Maximum load), then for $Q = Q_{Min}$ (light load condition), duty cycle has to be reduced in order to get the same voltage gain M. If the reduced duty cycle (denoted by d_0 in Fig. 4.13) is less than practical ZVS duty cycle D_{ZVS} then ZVS is lost and converter could be damaged. Therefore, the first selection of the F, Q_{Max}, and transformer turns ratio has to be done in a way that the obtained d_0 for the Q_{Min} does not become smaller than D_{ZVS}. In other words, the gain value with $d = D_{ZVS}$ at $Q = Q_{Min}$ (denoted by M_{ZVS}) has to be smaller than or equal to the gain value with $d = 50\%$, at $Q = Q_{Max}$ (denoted by M_{Max}) to ensure that SRC always operates with ZVS. In order to have a better insight into the ZVS

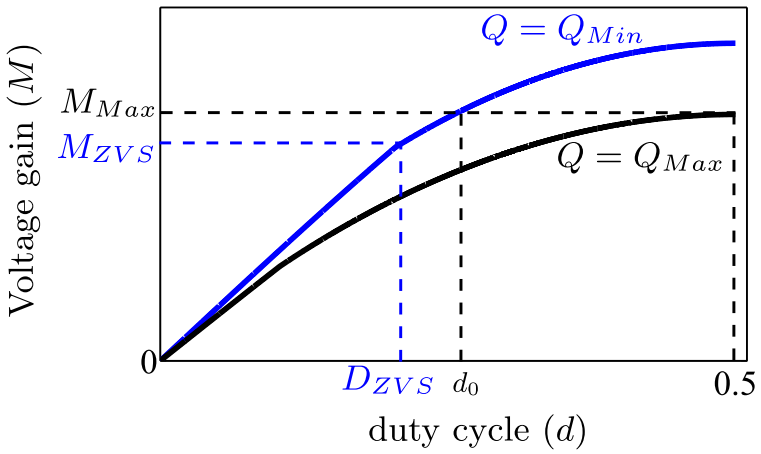

FIGURE 4.13: The voltage gain characteristic versus duty cycle for constant F ($Q_{Max} > Q_{Min}$).

range of the SRC with variable load, a new characteristic for SRC is defined which will be called Gain Ratio (M_r) from now on. According to discussion in previous part the ZVS operation could be guaranteed for all the loads if M_{Max} is larger than M_{ZVS}. Therefore, Gain Ratio M_r is defined as:

$$M_r = \frac{M_{Max}}{M_{ZVS}} = \frac{M\left(d = 0.5, Q = Q_{Max}, F\right)}{M\left(d = D_{ZVS}, Q = Q_{Min}, F\right)}. \tag{4.49}$$

$$Q = \frac{Z_0}{n_t^2 R_L} = \frac{Z_0}{n_t^2 V_{dcout}^2} P \implies \frac{Q_{Max}}{Q_{Min}} = \frac{P_{Max}}{P_{Min}} = P_r. \tag{4.50}$$

Also D_{ZVS} could be obtained in terms of F, and Q_{Min} as discussed in section 4.2.2.Therefore, M_r is only a function of F, Q_{Max} and P_r. Furthermore, as it has been shown in section 4.1.1, Q_{Max} could be described as:

$$Q_{Max} = \frac{2F}{\pi M_{Max}} \left[-1 + \sqrt{1 + (1 - M_{Max}^2) \tan^2(\frac{\pi}{2F})} \right]. \tag{4.51}$$

In which M_{Max} is obtained from the SRC gain constraint as:

$$M_{Max} = \frac{n_t V_{dcout}}{V_i}. \tag{4.52}$$

As V_{dcout} and V_i are given design specifications, using (4.51) and (4.52), Q_{Max} could be described in terms of F and n_t. Therefore, Gain Ratio of the SRC M_r is a characteristic that is a function of F, n_t, and P_r:

$$M_r = \frac{M_{Max}}{M_{ZVS}} = \frac{f(F, n_t)}{g(F, n_t, P_r)} \tag{4.53}$$

Even though the total gain of the converter is constant and given as a design requirement, various sets of resonant tank gain (M) and transformer turns ratio (n_t) could be used to generate the required total gain. As the resonant tank gain (M) is limited to the maximum value of 1 then a maximum allowable transformer turns ratio (n_t^{Max}) is obtained by letting $M_{Max} = 1$ in (4.52) as:

$$n_t^{Max} = \frac{V_i}{V_{dcout}}. \tag{4.54}$$

In order to normalize the transformer turns ratio, n_t is described as the fraction of the maximum n_t as:

$$n_{pu} = \frac{n_t^{Max}}{n_t}. \tag{4.55}$$

In order to show the effect of P_r on gain ratio M_r, Fig. 4.14 is sketched in $M_r - F$ plane for various P_r values with $n_{pu} = 1.4$. If $M_r \geq 1$, then SRC operates with ZVS, and if $M_r < 1$ then ZVS operation will be lost for light load condition. The first observation from Fig. 4.14 is that, by increasing P_r the gain ratio decreases. In fact,

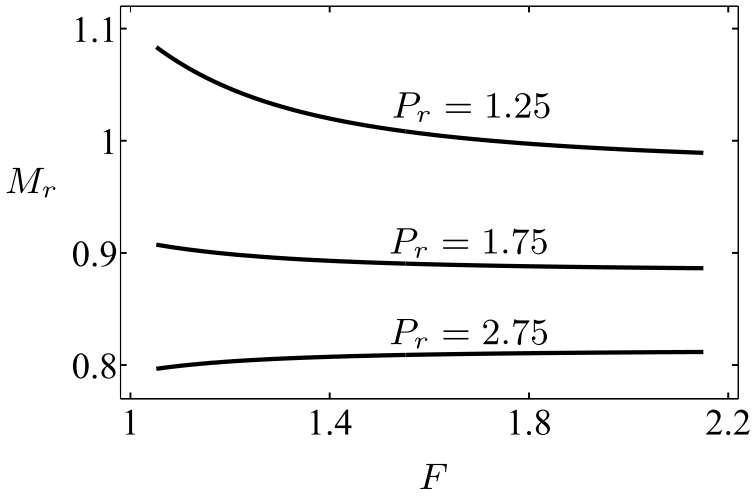

FIGURE 4.14: The gain ratio characteristic in $M_r - F$ plane for $n_{pu} = 1.4$ and different P_r values.

Fig. 4.14 proposes that in the SRC, larger variations in load results in smaller ZVS range.

The second observation from Fig. 4.14 is that the slope $\frac{\partial M_r}{\partial F}$ is negative for small P_r values and then it becomes positive for larger P_r values. Also for large F values, $\frac{\partial M_r}{\partial F} \rightarrow 0$, and the gain ratio characteristic versus F becomes a flat line. In other words, for smaller P_r values increasing F results in ZVS range reduction, until F reaches large values where the ZVS reduction will be saturated.

The other parameter that determines the gain ratio characteristic is the transformer turns ratio (n_{pu}). Figure 4.15 and 4.16 show the effect of n_{pu} on the variable load SRC behavior for $P_r = 1.5$ and $P_r = 2.5$ respectively.

It can be observed from Fig. 4.15 that the gain ratio M_r and consequently the ZVS range is increased by increasing n_{pu} and for the $P_r = 1.5$, n_{pu} has to be at least 2 or larger to guarantee the ZVS operation for all loads. However, Fig. 4.15 shows that the minimum n_{pu} to get the ZVS for a SRC with $P_r = 2.5$ is 4.5 or larger. Then it

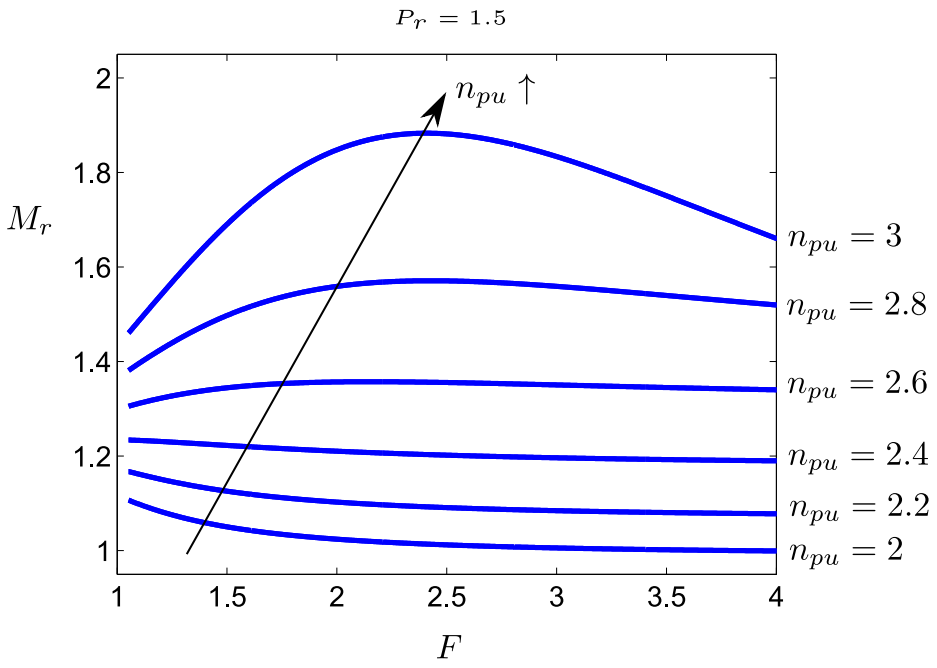

FIGURE 4.15: The gain ratio characteristic in $M_r - F$ plane for $P_r = 1.5$ and different n_{pu} values.

can be concluded that in SRC, n_{pu} has to be increased to get ZVS for a larger load variation range. The physical interpretation is that increasing n_{pu} results in lower required M values or accordingly more inductive circuit and larger current phase lag leading to a larger ZVS range.

Also $\frac{\partial M_r}{\partial F}$ is important for design purposes, because the optimum F is the one that has the largest M_r value and consequently ZVS range. Therefore, $\frac{\partial M_r}{\partial F}$ is analyzed to find the optimum F value that gives the largest ZVS range. It can be observed from Fig. 4.15 that the slope of $\frac{\partial M_r}{\partial F}$ for smaller n_{pu} is negative, and it becomes positive for larger n_{pu} values. However, in Fig. 4.16 the slope of $\frac{\partial M_r}{\partial F}$ is always positive that is because of large P_r value for this figure. In fact, increased P_r leads into larger n_{pu} values to get ZVS and as increasing P_r and n_{pu} value results in positive $\frac{\partial M_r}{\partial F}$ for large P_rs it can be stated that the gain ratio curves will always be similar to Fig. 4.16.

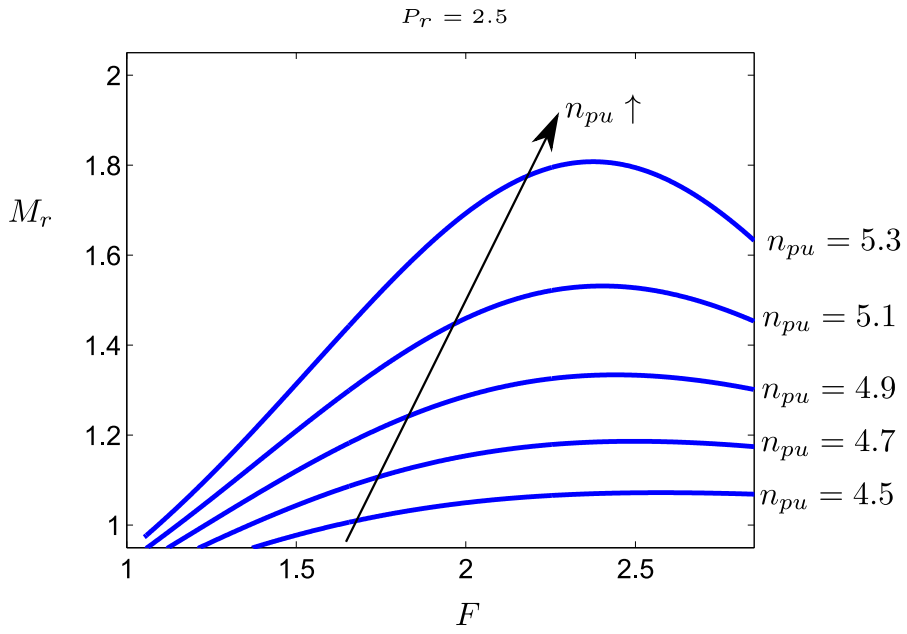

FIGURE 4.16: The gain ratio characteristic in $M_r - F$ plane for $P_r = 2.5$ and different n_{pu} values.

Therefore, the proposed design procedure for fixed frequency SRC will be based on Fig. 4.16.

Figure 4.16 shows that there is a specific F, that the largest gain ratio or ZVS range occurs at that F. In fact, for some large n_{pu} values the gain ratio has a parabolic shape in $M_r - F$ plane. If theoretical ZVS duty cycle d_{ZVS} was used instead of practical ZVS duty cycle D_{ZVS}, then the gain characteristics would always have a positive $\frac{\partial M_r}{\partial F}$ without any specific F value for which maximum gain occurs. The current zero crossing angle θ could almost reach $\frac{\pi}{2}$ for large F values. Then the theoretical d_{ZVS} could be reduced up to zero and in this case, theoretically the converter could convert the input voltage into output voltage for almost any load. However, in practice when θ reaches $\frac{\pi}{2}$ a small duty ratio has to be non zero to ensure that there is negative current in the whole switching period. As shown in section 4.2.2 the accuracy of

D_{ZVS} is for $d_{ZVS} > 0.05$. Therefore, smallest d_{ZVS} which leads to largest ZVS range is assumed to be 0.05.

In most of the voltage regulation applications, in addition to the load variations, the input voltage is changed in a range and the output voltage is needed to be fixed. Thus, the resonant tank gain (M) has to be changed in a range to support the fixed output voltage. Therefore, according to the Fig. 4.13, the voltage gain has to be greater than the required maximum to minimum voltage gain which results in:

$$M_r \geq \frac{V_i^{Max}}{V_i^{Min}}. \tag{4.56}$$

Where $\frac{V_i^{Max}}{V_i^{Min}}$ is the input voltage ratio that will be denoted by V_r from here on. In following sections V_r is a given value as design requirement.

Now that all the characteristics of the SRC with variable load and input voltage are analyzed, the design procedure could be proposed according to the obtained curves. As large P_r values are common in the most of applications, the design procedure is proposed based on Fig. 4.16. The discussion for lower P_r value is presented separately.

If the n_t, L, and C values are determined then the design is complete. The flowchart shown in Fig. 4.17 is proposed for the design of fixed frequency SRC. Generally ZVS range is a function of n_t and converter tank parameters. As using n_t for ZVS range increase results in larger circulating current, for each n_t, the maximum allowable ZVS range should be used in design. The maximum ZVS range for a given n_t occurs where $d_{ZVS}(F, Q) = 0.05$. This is one equation in terms of F and Q. The second equation is obtained from (4.56) which states that converter should be able to cover the whole input voltage range and power range by changing the duty cycle from $d = 50\%$ to

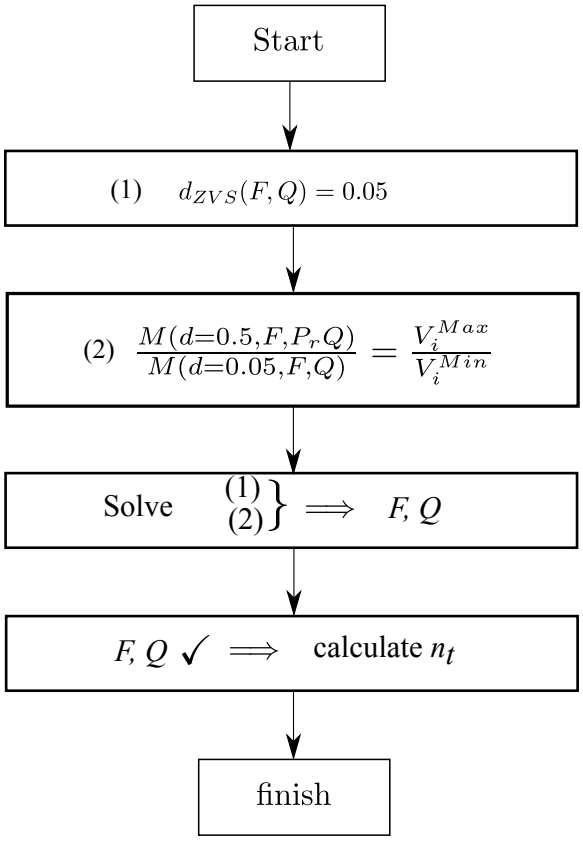

FIGURE 4.17: The design flowchart of the fixed frequency (variable duty ratio) SRC.

$d = d_{ZVS}$. Solving these two equations, F and Q values required for tank selection are obtained. Now having F and Q values, n_t is selected using the following formula. This formula guarantees that converter is able to convert the minimum input voltage to the required output voltage using the calculated tank in previous step:

$$n_t = \frac{V_i^{Min}}{V_{dcout}} \left(\frac{2F}{\pi Q}\right) \frac{AB\sqrt{A^2+B^2-1}-B^2}{A^2+B^2}. \tag{4.57}$$

$$A = sec\left(\frac{\pi}{2F}\right) \qquad B = \left(\frac{\pi P_r Q}{2F}\right) csc\left(\frac{\pi}{2F}\right). \tag{4.58}$$

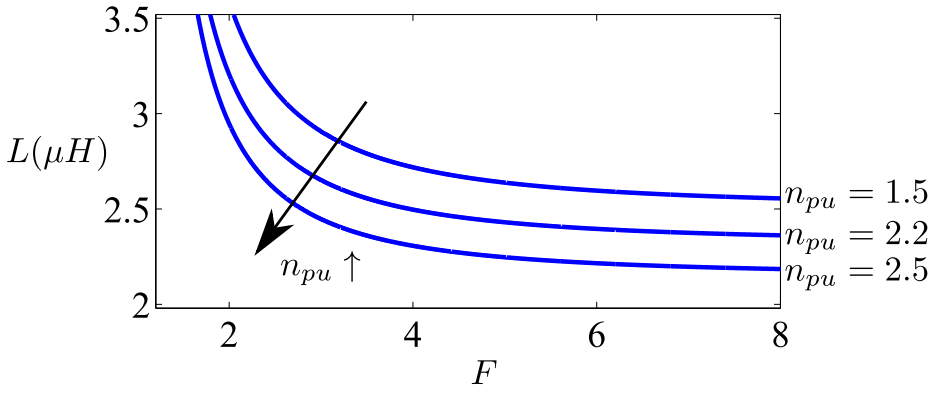

FIGURE 4.18: Inductance of the designed SRC versus F with $P_r = 1.5$ and different n_{pu} values.

For the small P_r and V_r values, $\frac{\partial M_r}{\partial F}$ is always negative (like $V_r = 1.1$, and $P_r = 1.5$ as shown in Fig. 4.15) and the smallest possible n_{pu} occurs for the F values close to 1. However, as shown in Fig. 4.18 selecting F close to 1 could result in large L values. In order to find L and C values corresponding to each curve in $M_r - F$ plane, $L - F$ and $C - F$ characteristics are sketched for the n_{pu} values used in $M_r - F$ plane. Having n_{pu} the required gain value is obtained:

$$M_{req} = \frac{1}{n_{pu}}. \tag{4.59}$$

Then Q value corresponding to each F is determined as:

$$Q = \frac{2F}{\pi M_{req}} \left[-1 + \sqrt{1 + \left(1 - M_{req}^2\right) \tan^2\left(\frac{\pi}{2F}\right)} \right]. \tag{4.60}$$

Now that Q value for each F is known, L and C value corresponding to each F is obtained as the following:

$$L = \frac{n_t^2 R_L}{\omega_s} \times QF. \tag{4.61}$$

$$C = \left(\omega_s n_t^2 R_L\right)^{-1} \times \frac{F}{Q}. \tag{4.62}$$

Figure 4.18 shows the L versus F for the $P_r = 1.5$ and some n_{pu} values. As it can be observed L is a homographic function of F and increases significantly as F becomes closer to 1. Therefore, selecting the smallest possible n_{pu} that could provide the desired V_r could result in large L values. However, if larger n_{pu} values that could provide the desired V_r are used, then a smaller L is obtained. Therefore, n_{pu} is increased up to an amount that the corresponding L becomes equal to the leakage inductance and use of external inductance is avoided. However, selecting large n_{pu} and consequently F value, results in larger capacitance C for the design. Figure 4.19 shows C versus F for $P_r = 1.5$ and some n_{pu} values. Also Fig. 4.20 shows the capacitor voltage stress obtained for $P_r = 1.5$ and some n_{pu} values. It could be observed that the required capacitance increases as F is increased. However, the voltage stress on the capacitor decreases as F increases. Thus for large selection of n_{pu}, large C is required, but reduced voltage stress makes it possible to find the desired capacitor in the market.

Based on the discussion above, the following three steps are proposed for L, C, and n_{pu} selection in the case $\frac{\partial M_r}{\partial F}$ is always negative for the given P_r and V_r value:

1. In the $M_r - F$ curves sketched for the given P_r value, find the smallest possible n_{pu} value that could provide the desired V_r value. If L value obtained for the selected n_{pu} and F value form the $L - F$ characteristic is equal to the leakage inductance then the design is complete. If obtained L is larger than the leakage inductance then go to step 2. (note that if the obtained L is smaller than the leakage inductance then it is not practically possible to design a SRC that oprate with ZVS for the specified P_r and V_r requirements.)

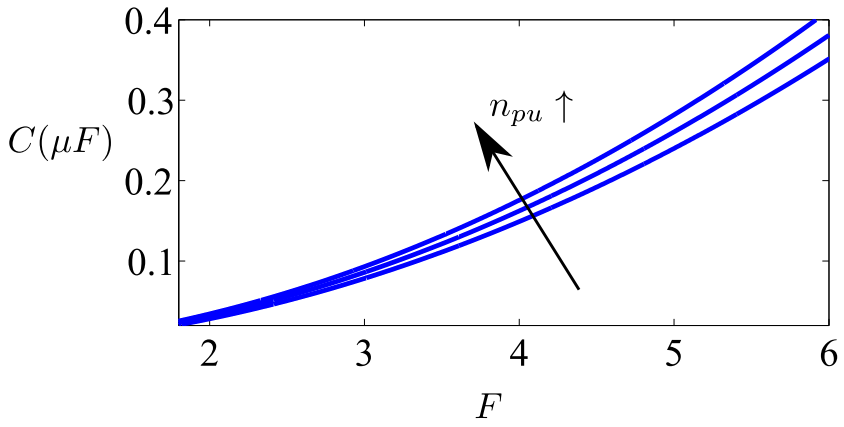

FIGURE 4.19: Capacitance C of the designed SRC versus F with $P_r = 1.5$ and $n_{pu} = 1.5,\ 2.2,\ 2.5$.

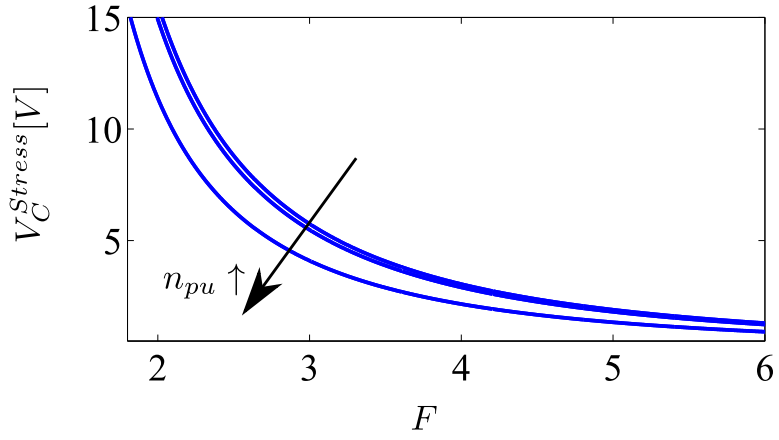

FIGURE 4.20: Maximum capacitor voltage stress of the designed SRC versus F with $P_r = 1.5$ and $n_{pu} = 1.5,\ 2.2,\ 2.5$.

2. Increase the n_{pu} value from the value selected in the previous step until the obtained n_{pu} and corresponding F value results in $L = L_{leakage}$. Derive the required C and its stress for the obtained n_{pu} and F value. If the required capacitor is provided by the vendors, then the design is complete and the SRC is designed without any external inductance but with negligible increase in the current. If the designed capacitor is not available in the market go to step 3.

3. Decrease n_{pu} value from the one obtained in step 2 until the capacitance required

for the design becomes equal to the largest possible capacitance that is available in the market. (note that if the reduced n_{pu} becomes smaller than the n_{pu} obtained in step 1 then it is not practically possible to design a SRC that oprate with ZVS for the specified P_r and V_r requirements.)

It is important to note that the design procedure presented for ZVS fixed frequency SRC is based on the closed form and accurate formula for d_{ZVS}. Formula for ZVS range boundary is obtained for the first time in the literature and previous design procedures all are based on designer's experience to select the required parameters for the application.

4.3 Variable Frequency and Variable Duty Cycle SRC

As it has been shown in the previous sections, the pulse frequency control method leads to large variation in F and consequently less power density is achieved. For the fixed frequency control method, extension of the ZVS range comes at the expense of selecting sub-optimal transformer turns ratio which causes excessive conduction losses. Furthermore, none of the above mentioned controls could cover the no-load condition. Thus a new control and design approach is presented here that uses both SRC switching frequency and duty cycle for the voltage regulation purpose. Also as discussed in DCM analysis section (3.2), SRC has ZCS in DCM because the current becomes zero at switching instants. Therefore, SRC is still operating with soft switching even if it enters DCM, and DCM could be used to extend the range of load and input voltage. For an optimized design of SRC tank parameters can be selected in a

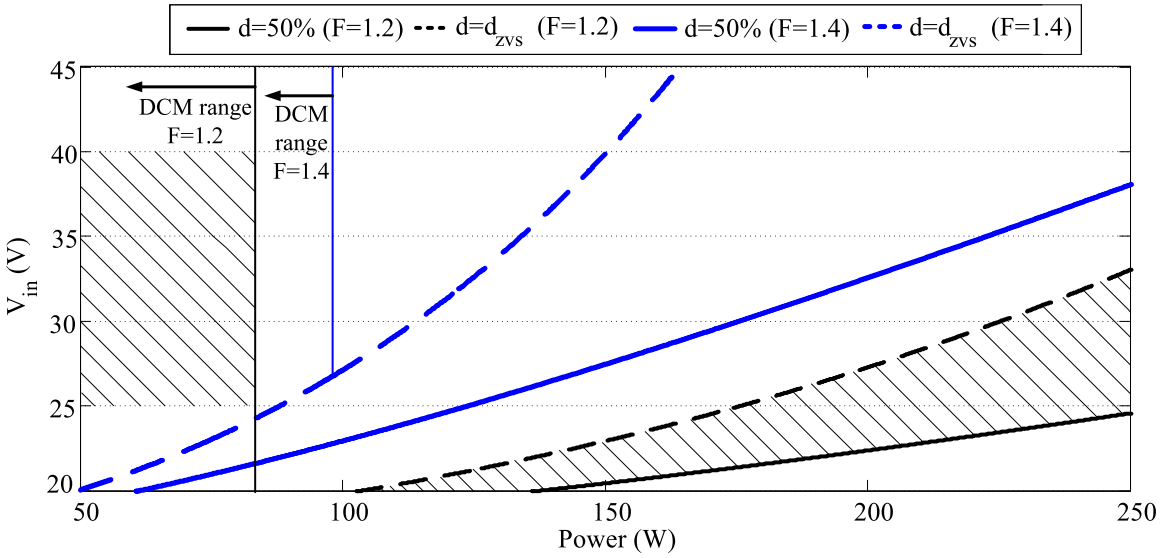

FIGURE 4.21: SRC operation boundaries for $F = 1.2$ and $F = 1.4$

way that for any loading condition converter operates in either ZVS mode ($d > d_{ZVS}$) or in ZCS mode in DCM. Consider the following SRC design problem. The output voltage must be fixed at $400V$, while input voltage range is $25V$ to $40V$, and power could vary from zero to $250W$. For such a large conversion ratio transformer turns is selected to be $1 : 24$ and for practical considerations $Z_0 = \sqrt{\frac{L}{C}}$ is selected to be 2.5Ω. Now that transformer turns ratio and output voltage are determined, every power level presents by a Q. Therefore, d and F are two control variables that could be used to fix the output at $400V$ despite the input voltage and power variations.

As $d = 50\%$ is the maximum duty ratio that provides the largest M, then for every F the smallest input voltage that could be converted to $400V$ could be derived using (3.26). Also the ZVS violation duty cycle, d_{ZVS}, and its corresponding input voltage could be obtained for every F using (3.28) and (3.26) respectively. Figure 4.21 shows these boundaries for two values of F. Converter operates with ZVS between these two boundaries, and its DCM operation boundary is the Q value obtained using (3.29)

and its corresponding power level. For $F = 1.2$, the striped regions in right and left show the ZVS and DCM operation regions respectively. SRC has soft switching operation for these regions but as it can be seen this single frequency does not cover all of the desired area. Thus a larger F value such as $F = 1.4$ as shown in the figure, should be added to extend the area for both ZVS and DCM operation regions. Using this procedure the SRC which is able to operate under soft switching that covers all the desired range is designed with four F values as $F_1 = 1.2$, $F_2 = 1.28$, $F_3 = 1.4$ and $F_4 = 1.54$.

4.4 Summary

Design of both variable duty cycle and variable frequency control SRC is discussed in this section. For the frequency controlled SRC it is shown that the transformer ratio selection is a compromise between conduction losses and full turn on ZVS. The optimum transformer ratio is n_t^{Max}, however, smaller n_t might be selected to achieve full turn on ZVS at the expense of increased s=conduction losses. After transformer selection, tank elements and snubber capacitance could be selected from maximum capacitor voltage stress and full turn on ZVS conditions respectively. For the fixed frequency SRC, new characteristics of practical ZVS duty cycle (D_{ZVS}) and Gain Ratio (M_r) are defined to find the necessary condition for ZVS operation for the whole load and input voltage range. It is shown that the extension of ZVS range to full range is obtained by increasing the conduction loss. Also optimum F and n_t selection criteria is described using the Gain Ratio characteristics.

Chapter 5

Conclusion

5.1 Major Contributions

In this thesis a parametric and accurate analysis and design tool is proposed that is applicable to a large class of switched mode power converters including resonant converters. The proposed methodology is adopted to tackle the analysis and design of SRC. The main contributions and conclusions of the thesis is summarized here.

(i) A Laplace based theorem (LBT) is proposed and proved to find the closed form steady state periodic solution of a dynamic system with discontinuous and periodic inputs. The theorem predicts the steady state initial conditions using the Laplace transform of the input function.

(ii) LBT is utilized to develop an effective analysis and design tool for converters that could be modeled by an ODE with periodic input. The proposed analysis

tool is applied to a few power circuit, and Buck converter examples and the accurate and parametric solutions are derived.

(iii) The variable duty cycle full bridge series resonant converter has been analyzed using the proposed method. Both CCM and DCM operations are analyzed and explicit, parametric and exact equations are found for converter characteristics and waveforms. It is shown that unlike the conventional approaches, the proposed analysis tool provides accurate closed form parametric solutions and equations for converter boundary conditions like ZVS range, DCM criteria, etc.

(iv) Simulation and experimental results are shown to validate the accuracy of the proposed method.

(v) Using the insight provided by the proposed method, different trade-offs in the design of both fixed frequency and frequency modulated SRC are discussed . The explicit equations for the selection of SRC parameters in each case are derived. The systematic and optimized design approach for each case is described using the transparent design flowchart.

5.2 Future Work

There are many directions that this research could go as the next stage of the study. Below is a brief list of a few possible future work:

(i) In this thesis the steady state response of converters are analyzed. With some mathematical manipulations anther theorem could be proposed for transient response analysis. The transient response of the system could be used for dynamic modeling and control of a large class of converters.

(ii) As the proposed method is general and could analyze the high order resonant converters as well, then as the next stage of the research the proposed method could be used for exact and parametric analysis of LLC and LCC resonant converters. Due to the improved characteristics, LLC and LCC converters have many practical applications, however, there is no accurate analysis available in the literature for such converters.

(iii) One of the main issues for the DC/DC resonant converters is their Synchronous Rectifier stage and its gating. As the proposed method provides parametric equations for the current zero crossing, an accurate observer based controller could be designed based on the obtained equations that eases the measurement requirements.

Bibliography

[1] Marian K Kazimierczuk and Dariusz Czarkowski. *Resonant power converters*. John Wiley & Sons, 2012.

[2] Ned Mohan and Tore M Undeland. *Power electronics: converters, applications, and design*. John Wiley & Sons, 2007.

[3] Robert W Erickson and Dragan Maksimovic. *Fundamentals of power electronics*. Springer Science & Business Media, 2007.

[4] D. J. Perreault, J. Hu, J. M. Rivas, Y. Han, O. Leitermann, R. C. N. Pilawa-Podgurski, A. Sagneri, and C. R. Sullivan. Opportunities and challenges in very high frequency power conversion. In *Applied Power Electronics Conference and Exposition, 2009. APEC 2009. Twenty-Fourth Annual IEEE*, pages 1–14, Feb 2009. doi: 10.1109/APEC.2009.4802625.

[5] G. Hua and F. C. Lee. Soft-switching techniques in pwm converters. *IEEE Transactions on Industrial Electronics*, 42(6):595–603, Dec 1995. ISSN 0278-0046. doi: 10.1109/41.475500.

[6] X. Li and A. K. S. Bhat. Analysis and design of high-frequency isolated dual-bridge series resonant dc/dc converter. *IEEE Transactions on Power Electronics*, 25(4):850–862, April 2010. ISSN 0885-8993. doi: 10.1109/TPEL.2009.2034662.

[7] Bo Yang, F. C. Lee, A. J. Zhang, and Guisong Huang. *llc* resonant converter for front end dc/dc conversion. In *Applied Power Electronics Conference and Exposition, 2002. APEC 2002. Seventeenth Annual IEEE*, volume 2, pages 1108–1112 vol.2, 2002. doi: 10.1109/APEC.2002.989382.

[8] R. Redl, B. Molnar, and N. O. Sokal. Class e resonant regulated dc/dc power converters: Analysis of operations, and experimental results at 1.5 mhz. *IEEE Transactions on Power Electronics*, PE-1(2):111–120, April 1986. ISSN 0885-8993. doi: 10.1109/TPEL.1986.4766289.

[9] X. Fang, H. Hu, Z. J. Shen, and I. Batarseh. Operation mode analysis and peak gain approximation of the llc resonant converter. *IEEE Transactions on Power Electronics*, 27(4):1985–1995, April 2012. ISSN 0885-8993. doi: 10.1109/TPEL.2011.2168545.

[10] G. Ivensky, S. Bronshtein, and A. Abramovitz. Approximate analysis of resonant llc dc-dc converter. *IEEE Transactions on Power Electronics*, 26(11):3274–3284, Nov 2011. ISSN 0885-8993. doi: 10.1109/TPEL.2011.2142009.

[11] P. T. Krein, J. Bentsman, R. M. Bass, and B. C. Lesieutre. On the use of averaging for the analysis of power electronic systems. In *Power Electronics Specialists Conference, 1989. PESC '89 Record., 20th Annual IEEE*, pages 463–467 vol.1, Jun 1989. doi: 10.1109/PESC.1989.48523.

[12] S. R. Sanders, J. M. Noworolski, X. Z. Liu, and G. C. Verghese. Generalized averaging method for power conversion circuits. *IEEE Transactions on Power Electronics*, 6(2):251–259, Apr 1991. ISSN 0885-8993. doi: 10.1109/63.76811.

[13] Numerical state-space average-value modeling of pwm dc-dc converters operating in dcm and ccm. *IEEE Transactions on Power Electronics*, 21(4):1003–1012, July 2006. ISSN 0885-8993. doi: 10.1109/TPEL.2006.876848.

[14] R. J. King and T. A. Stuart. Small-signal model for the series resonant converter. *IEEE Transactions on Aerospace and Electronic Systems*, AES-21(3):301–319, May 1985. ISSN 0018-9251. doi: 10.1109/TAES.1985.310560.

[15] Robert L Steigerwald. A comparison of half-bridge resonant converter topologies. *Power Electronics, IEEE Transactions on*, 3(2):174–182, 1988.

[16] Andrew J Forsyth, Gillian Ward, Stefan V Mollov, et al. Extended fundamental frequency analysis of the lcc resonant converter. *Power Electronics, IEEE Transactions on*, 18(6):1286–1292, 2003.

[17] J.A. Martin-Ramos, J. Diaz, A.M. Pernia, J.M. Lopera, and F. Nuno. Dynamic and steady-state models for the prc-lcc resonant topology with a capacitor as output filter. *Industrial Electronics, IEEE Transactions on*, 54(4):2262–2275, Aug 2007. ISSN 0278-0046. doi: 10.1109/TIE.2007.894763.

[18] A.K.S. Bhat. A generalized steady-state analysis of resonant converters using two-port model and fourier-series approach. *Power Electronics, IEEE Transactions on*, 13(1):142–151, Jan 1998. ISSN 0885-8993. doi: 10.1109/63.654968.

[19] Jia Hou, Qianhong Chen, Xiaoyong Ren, Xinbo Ruan, Siu-Chung Wong, and C.K. Tse. Precise characteristics analysis of series/series-parallel compensated

contactless resonant converter. *Emerging and Selected Topics in Power Electronics, IEEE Journal of*, 3(1):101–110, March 2015. ISSN 2168-6777. doi: 10.1109/JESTPE.2014.2320524.

[20] P. Jain, H. Soin, and M. Cardella. Constant frequency resonant dc/dc converters with zero switching losses. *Aerospace and Electronic Systems, IEEE Transactions on*, 30(2):534–544, Apr 1994. ISSN 0018-9251. doi: 10.1109/7.272276.

[21] A. Safaee, M. Karimi-Ghartemani, P. K. Jain, and A. Bakhshai. Time-domain analysis of a phase-shift-modulated series resonant converter with an adaptive passive auxiliary circuit. *IEEE Transactions on Power Electronics*, 31(11):7714–7734, Nov 2016. ISSN 0885-8993. doi: 10.1109/TPEL.2016.2557725.

[22] K. D. T. Ngo. Analysis of a series resonant converter pulse width-modulated or current-controlled for low switching loss. *IEEE Transactions on Power Electronics*, 3(1):55–63, Jan 1988. ISSN 0885-8993. doi: 10.1109/63.4331.

[23] E. X. Yang, F. C. Lee, and M. M. Jovanovic. Small-signal modeling of series and parallel resonant converters. pages 785–792, Feb 1992. doi: 10.1109/APEC.1992.228333.

[24] Hai-Jiang Jiang, G. Maggetto, and P. Lataire. Steady-state analysis of the series resonant dc-dc converter in conjunction with loosely coupled transformer-above resonance operation. *IEEE Transactions on Power Electronics*, 14(3):469–480, May 1999. ISSN 0885-8993. doi: 10.1109/63.761691.

[25] Ramesh Oruganti and Fred C Lee. Resonant power processors, part i—state plane analysis. *Industry Applications, IEEE Transactions on*, (6):1453–1460, 1985.

[26] AF Witulski and RW Erickson. Design of the series resonant converter for minimum component stress. *Aerospace and Electronic Systems, IEEE Transactions on*, (4):356–363, 1986.

[27] R. Beiranvand. Analysis of a switched-capacitor converter above its resonant frequency to overcome voltage regulation issue of resonant sccs. *IEEE Transactions on Industrial Electronics*, PP(99):1–1, 2016. ISSN 0278-0046. doi: 10.1109/TIE.2016.2561270.

[28] I Batarseh. State-plane approach for the analysis of half-bridge parallel resonant converters. *IEE Proceedings-Circuits, Devices and Systems*, 142(3):200–204, 1995.

[29] Adam J Gilbert, Christopher M Bingham, David Stone, Martin P Foster, et al. Normalized analysis and design of lcc resonant converters. *Power Electronics, IEEE Transactions on*, 22(6):2386–2402, 2007.

[30] Z. Hu, L. Wang, H. Wang, Y. F. Liu, and P. C. Sen. An accurate design algorithm for llc resonant converters—part i. *IEEE Transactions on Power Electronics*, 31 (8):5435–5447, Aug 2016. ISSN 0885-8993. doi: 10.1109/TPEL.2015.2496333.

[31] Z. Hu, L. Wang, Y. Qiu, Y. F. Liu, and P. C. Sen. An accurate design algorithm for llc resonant converters—part ii. *IEEE Transactions on Power Electronics*, 31 (8):5448–5460, Aug 2016. ISSN 0885-8993. doi: 10.1109/TPEL.2015.2496179.

[32] Jean-Pierre Vandelac and Phoivos D Ziogas. A dc to dc pwm series resonant converter operated at resonant frequency. *Industrial Electronics, IEEE Transactions on*, 35(3):451–460, 1988.

[33] Yash Veer Singh, Kanakasabai Viswanathan, Rajendra Naik, Juan A Sabate, and Rixin Lai. Analysis and control of phase-shifted series resonant converter operating in discontinuous mode. In *Applied Power Electronics Conference and Exposition (APEC), 2013 Twenty-Eighth Annual IEEE*, pages 2092–2097. IEEE, 2013.

[34] James F Lazar and Robert Martinelli. Steady-state analysis of the llc series resonant converter. In *Applied Power Electronics Conference and Exposition, 2001. APEC 2001. Sixteenth Annual IEEE*, volume 2, pages 728–735. IEEE, 2001.

[35] Ying-Chun Chuang, Yu-Lung Ke, Hung-Shiang Chuang, and Hung-Kun Chen. Implementation and analysis of an improved series-loaded resonant dc–dc converter operating above resonance for battery chargers. *Industry Applications, IEEE Transactions on*, 45(3):1052–1059, 2009.

[36] AC Sanchez, Nelson L Diaz, HR Chamorro, and JF Bayona. A novel analysis and design assessment for series resonant converters operating above resonance. In *Industry Applications (INDUSCON), 2012 10th IEEE/IAS International Conference on*, pages 1–6. IEEE, 2012.

[37] Zhigang Liang, Rong Guo, Jun Li, and Alex Q Huang. A high-efficiency pv module-integrated dc/dc converter for pv energy harvest in freedm systems. *Power Electronics, IEEE Transactions on*, 26(3):897–909, 2011.

[38] Oscar Lucia, JoséM Burdío, Ignacio Millán, Jesũs Acero, and Diego Puyal. Load-adaptive control algorithm of half-bridge series resonant inverter for domestic induction heating. *Industrial Electronics, IEEE Transactions on*, 56(8):3106–3116, 2009.

[39] D.J. Tschirhart and P.K. Jain. Design procedure for high-frequency operation of the modified series-resonant apwm converter to reduce size and circulating current. *Power Electronics, IEEE Transactions on*, 27(10):4181–4191, Oct 2012. ISSN 0885-8993. doi: 10.1109/TPEL.2012.2191420.

[40] Sanjaya Maniktala. *Switching Power Supplies A-Z*. Elsevier, 2012.